

1 WIDE BAND GAP KESTERITE ABSORBERS FOR THIN FILM SOLAR CELLS:
2 POTENTIAL AND CHALLENGES FOR THEIR DEPLOYMENT IN TANDEM DEVICES

3
4 Bart Vermang^{1,2,3}, Guy Brammertz^{1,2,3}, Marc Meuris^{1,2,3}, Thomas Schnabel⁴, Erik Ahlswede⁴,
5 Leo Choubrac⁵, Sylvie Harel⁵, Christophe Cardinaud⁵, Ludovic Arzel⁵, Nicolas Barreau⁵,
6 Joop van Deelen⁶, Pieter-Jan Bolt⁶, Patrice Bras⁷, Yi Ren⁷, Eric Jaremalm⁷, Samira Khelifi^{8,9},
7 Sheng Yang⁸, Johan Lauwaert⁸, Maria Batuk¹⁰, Joke Hadermann¹⁰, Xeniya Kozina¹¹,
8 Evelyn Handick¹¹, Claudia Hartmann¹¹, Dominic Gerlach¹², Asahiko Matsuda¹³,
9 Shigenori Ueda^{14,15}, Toyohiro Chikyow^{12,13}, Roberto Félix¹¹, Yufeng Zhang^{11,16},
10 Regan G. Wilks^{11,17}, and Marcus Bär^{11,17,18,19}

11
12 ¹imec division IMOMEK – partner in Solliance, Wetenschapspark 1, 3590 Diepenbeek,
13 Belgium

14 ²Hasselt University – partner in Solliance, Martelarenlaan 42, 3500 Hasselt, Belgium

15 ³EnergyVille, Thorpark 8320, 3600 Genk, Belgium

16 ⁴ZSW, Meitnerstrasse 1, 70563 Stuttgart, Germany

17 ⁵Institut des Matériaux Jean Rouxel (IMN), Université de Nantes, CNRS, 2 rue de la
18 Houssinière, 44322 Nantes, France

19 ⁶TNO – partner in Solliance, High Tech Campus 21, 5656 AE Eindhoven, The Netherlands

20 ⁷Midsummer AB, Elektronikhöjden 6, 175 43 Järfälla, Sweden

21 ⁸Department of Electronics and Information Systems (ELIS), Ghent University,
22 Technologiepark Zwijnaarde 15, 9052 Gent, Belgium

23 ⁹Department of Solid State Sciences, Ghent University, Krijgslaan 281-S1, 9000 Gent,
24 Belgium

25 ¹⁰Electron Microscopy for Materials Science (EMAT), University of Antwerp,
26 Groenenborgerlaan 171, 2020 Antwerp, Belgium

27 ¹¹Department Interface Design, Helmholtz-Zentrum Berlin für Materialien und Energie
28 GmbH (HZB), Hahn-Meitner-Platz 1, 14109 Berlin, Germany

29 ¹²International Center for Materials Nanoarchitectonics (MANA), National Institute for
30 Materials Science (NIMS), 1-1 Namiki, Tsukuba, Ibaraki 305-0044, Japan

1 ¹³Research and Services Division of Materials Data and Integrated System (MaDIS), National
2 Institute for Materials Science (NIMS), 1-1 Namiki, Tsukuba, Ibaraki 305-0044, Japan

3 ¹⁴Synchrotron X-ray Station at SPring-8, National Institute for Materials Science (NIMS), 1-1-
4 I Kouto, Sayo-cho, Hyogo 679-5148, Japan

5 ¹⁵Research Center for Advanced Measurement and Characterization, National Institute for
6 Materials Science (NIMS), 1-2-1, Sengen, Tsukuba, Ibaraki 305-0047, Japan

7 ¹⁶College of Physical Science and Technology, Xiamen University (XMU), 361005, Xiamen,
8 China

9 ¹⁷Energy Materials In-Situ Laboratory Berlin (EMIL), Helmholtz-Zentrum Berlin für
10 Materialien und Energie GmbH (HZB), Albert-Einstein-Str. 15, 12489, Berlin, Germany

11 ¹⁸Department of Chemistry and Pharmacy, Friedrich-Alexander-Universität Erlangen-
12 Nürnberg, 91058 Erlangen, Germany

13 ¹⁹Helmholtz-Institute Erlangen-Nürnberg for Renewable Energy (HI ERN),
14 Forschungszentrum Jülich, 91058 Erlangen, Germany

15

16 CORRESPONDING AUTHOR – Bart Vermang, Martelarenlaan 42, 3500 Hasselt, Belgium

1 BROADER CONTEXT

2 The power conversion efficiency of the dominant single junction photovoltaic technology is
3 approaching its theoretical limit. Further progress, with higher efficiencies and lower cost,
4 requires improving current technologies in new ways, whilst using cheap, abundant materials.
5 An approach to increase the efficiency is the construction of double junction solar cells
6 combining a top and bottom cell in a tandem device. If an established technology – such as
7 crystalline silicon – is used for the bottom cell, a relatively wide band gap material is needed
8 for the top cell. An ideal top cell would be low-cost and be made of abundant, non-toxic
9 materials. Typical top cell candidates that have been presented have some significant
10 drawbacks: Perovskite top cells, for example, contain toxic elements and have well-known
11 stability issues. III-V top cells are well studied for concentrators, but are too costly for tandem
12 applications. In this contribution, we report on our detailed fundamental analysis of a new
13 candidate absorber material, namely high band gap kesterite films. The Sn in the standard
14 $\text{Cu}_2\text{ZnSn}(\text{S,Se})_4$ kesterite structure is replaced by Ge (or Si), increasing the band gap to a level
15 where it is of interest in tandem configurations. This study describes the potential and the
16 challenges that are involved with the use of wide band gap kesterite absorbers in future
17 tandem devices.

18 19 ABSTRACT

20 This work reports on developments in the field of wide band gap Cu_2ZnXY_4 (with X = Sn, Si
21 or Ge, and Y = S, Se) kesterite thin film solar cells. An overview on recent developments and
22 the current understanding of wide band gap kesterite absorber layers, alternative buffer layers,
23 and suitable transparent back contacts is presented. $\text{Cu}_2\text{ZnGe}(\text{S,Se})_4$ absorbers with absorber
24 band gaps up to 1.7 eV have been successfully developed and integrated into solar cells.
25 Combining a CdS buffer layer prepared by an optimized chemical bath deposition process
26 with a 1.36 eV band gap absorber resulted in a record cell efficiency of 7.6 %, while the highest
27 open-circuit voltage of 730 mV could be obtained for a 1.54 eV band gap absorber and a
28 Zn(O,S) buffer layer. Employing InZnO_x or TiO_2 protective top layers on SnO_2 :In transparent
29 back contacts yields 85-90 % of the solar cell performance of reference cells (with Mo back
30 contact). These advances show the potential as well as the challenges of wide band gap
31 kesterites for future applications in high-efficiency and low-cost tandem photovoltaic devices.

32 33 KEYWORDS

34 Thin-film solar cells, wide band gap, kesterite, germanium, semi-transparent

1 I. INTRODUCTION

2 World-record single-junction solar cell efficiencies of monocrystalline silicon-wafer (Si) and
3 thin-film (TF) solar cells are 26.7 % and 22.9 % [1,2], respectively, thus approaching their
4 theoretical (Shockley-Queisser) limit of 30 % under standard illumination conditions [3]. One
5 approach to increase the efficiency of solar cells above this limit is the construction of tandem
6 devices. A tandem device consists of two solar cells: a wide band gap (E_G) solar cell (in which
7 the photovoltaically active absorber material has an optical band gap of 1.5-2.0 eV) harvests
8 the high-energy photons and a small band gap solar cell (in which the absorber has a band gap
9 of 1.0-1.5 eV) harvests the low-energy photons. This approach can lead to theoretical
10 efficiencies of up to 44 % under 1-sun illumination [4].

11 With a band gap of 1.1 eV [4], Si-wafer-based devices are the ideal bottom cell candidate, but
12 many prominent top cell candidates have issues related to abundance, toxicity, stability, or
13 cost [5]. Therefore, we consider kesterite-based devices as potential top cells for tandem
14 device applications, because $\text{Cu}_2\text{ZnSn}(\text{S,Se})_4$ -type kesterite solar cells are stable, made out of
15 abundant and non-toxic components, and already achieve relatively high performance [1].
16 Depending on the $[\text{S}]/([\text{S}]+[\text{Se}])$ composition, the band gap of the kesterite absorber can be
17 tuned between 1.0 and 1.5 eV [6]. Highest efficiencies for $\text{Cu}_2\text{ZnSn}(\text{S,Se})_4$ -based devices are
18 achieved when absorbers with band gaps between 1.1 and 1.2 eV are employed [7], which is
19 too low for efficient (top) tandem solar cell applications. However, (partially) replacing tin
20 atoms with silicon or germanium atoms has the potential to result in kesterite absorbers with
21 band gaps even above 1.5 eV [8,9]. This work aims to give an overview on the recent
22 development and current understanding of (i) these wide band gap kesterite absorber layers,
23 (ii) alternative (non-toxic) buffer layer candidate materials, and (iii) suitable transparent back
24 contacts (TBCs) allowing tandem configuration. A summary of recently published results is
25 complemented with new experimental findings and a theoretical study of the efficiency
26 potential of devices based on wide band gap kesterite absorbers. Thus, the paper aims at
27 covering all aspects of deploying kesterite wide-band gap absorbers as top cells in tandem
28 solar cell applications in order to identify inherent bottlenecks that may limit device
29 performance and present generally valid optimization approaches and first results to lay the
30 foundation and pave the way for future more detailed studies that undeniably have to follow.

32 2. EXPERIMENTAL, RESULTS, AND DISCUSSION

33 2.1. ABSORBER LAYER

34 First, we give an overview of the absorber layer formation, in which two main approaches are
35 applied, i.e. sequential evaporation (Section 2.1.1) and solution-based deposition (Section
36 2.1.2). The first approach (respective samples are henceforth called \rightarrow EVAP-sample) is more

1 convenient to study different metal components and is, therefore, used to investigate the
2 replacement of Sn atoms with Si or Ge in EVAP-Cu₂ZnSn(S,Se)₄ absorber layers; while in the
3 second approach (→ SOL-sample), the focus is on the replacement of Sn with Ge and the
4 optimization of the involved wet chemistry. Note that there will inherently be variations in
5 properties of the kesterite absorbers deposited by the different methods (i.e., using sequential
6 evaporation or solution-based deposition), however the findings that are presented in the
7 manuscript – while not exactly transferrable – mainly relate to universally relevant conditions
8 that will arise in cell production regardless of the absorber deposition method.

9 2.1.1. EVAPORATION-BASED PROCESS

10 The polycrystalline absorber layers are fabricated using a two-step vacuum-based approach;
11 see Figure S1. Soda lime glass (SLG) substrates of 1.3 mm thickness are used, on which a 150-
12 nm-thick Si(O,N) diffusion barrier is first deposited, followed by a 400-nm-thick Mo layer.
13 The thin Si(O,N) diffusion barrier is deposited in order to avoid the diffusion of elements
14 from the glass substrate into the absorber. Early tests have shown that the evaporated
15 absorber quality is better if this diffusion barrier is added. On top of this substrate, a multilayer
16 of different metals is deposited using a Pfeiffer PLS 500 evaporation system. For accurate layer
17 thickness control, a quartz microcrystal balance is used. This metal multilayer is then annealed
18 in an Annealsys As-One 150 rapid thermal annealing system that is equipped with a 10 % H₂Se
19 (diluted in N₂) gas line and a 100 % H₂S gas line. This way, the layers are selenized or sulfurized
20 under a continuous flow of H₂Se or H₂S. During this selenization/sulfurization step, a
21 polycrystalline layer is formed with typical grain sizes in the order of 0.5 to 1 μm.

22 2.1.1.1. Si-BASED COMPOUNDS

23 We have used metal layer stacks, including Si, to explore the possibility of fabricating EVAP-
24 Cu₂ZnSiSe₄, -Cu₂Zn(Si,Sn)Se₄, -Cu₂SiSe₃, -Cu₂SiS₃, -Cu₈SiSe₆, and -Cu₈SiS₆ layers [10].
25 Unfortunately, the Si appears to be largely unreactive at processing temperatures below
26 600 °C, which is the maximum temperature allowed for SLG substrates. Only EVAP-Cu₈SiSe₆
27 and EVAP-Cu₈SiS₆ could be produced in a reliable way, without significant presence of
28 secondary phases, leading to polycrystalline absorber layers with high-intensity
29 photoluminescence (PL) peaks at energies of 1.35 (for EVAP-Cu₈SiSe₆) and 1.84 eV (EVAP-
30 Cu₈SiS₆) [11]. However, no functioning solar cells could be fabricated with these absorber
31 layers, as the doping seemed to be too high (in the order of 10¹⁸ cm⁻³ or higher), and the
32 minority carrier lifetime seemed to be lower than 0.2 ns, leading to functioning diodes but no
33 photocurrent. One observation that could also explain the absence of any photoactivity is the
34 formation of SiO₂ during absorber processing. Figure 1 shows hard x-ray photoelectron
35 spectroscopy (HAXPES) survey spectra of an EVAP-Cu₈SiS₆ sample before (black) and after
36 (red) sulfurization treatment. Upon sulfurization, the O and Na (most likely diffused from the
37 SLG substrate) contents increase. The inset shows the region of the Si 2s and S 2p core level

1 lines compared to reference positions of silicon compounds [12]. The Si 2s line of the
2 sulfurized layer stack shifts to higher binding energies compared to the Si 2s peak before
3 sulfurization. The comparison with the reference positions indicates the conversion of Si-Si
4 into Si-S₂ and/or Si-O₂ bonds. The fact that the S 2p line can only be clearly observed on a
5 magnified (x 25) scale together with the high O 1s intensity for the sample after sulfurization,
6 however, suggests that the surface region of the sulfurized sample has mainly a SiO₂ character,
7 which would prevent efficient charge carrier transport.

8 2.1.1.2. Ge-BASED COMPOUNDS

9 For the fabrication of polycrystalline EVAP-Cu₂ZnGeSe₄ layers, we have used 180 nm of Ge,
10 125 nm of Zn and 170 nm of Cu as starting layers [13]. These layer thicknesses were chosen
11 in order to end up with a Zn-rich and Cu-poor composition of the absorber layer, with
12 Cu/(Zn+Ge) = 0.9 and Zn/Ge = 1.05. This metal stack was then selenized for 15 minutes in a
13 continuous flow of H₂Se at a temperature of 460 °C. The resulting absorber layer is
14 polycrystalline with a typical grain size in the order of 500 nm. Figure S2 shows a cross-section
15 scanning electron microscopy (SEM) image of a finished solar cell stack, exemplifying the grain
16 morphology of the absorber as well as the other layers of the solar cell stack. A Bragg
17 Brentano X-ray diffraction (XRD) measurement of a finished absorber layer on a Mo back
18 contact clearly shows the Cu₂ZnGeSe₄ peaks with a small contribution of a ZnSe secondary
19 phase, as a small shoulder of the main Cu₂ZnGeSe₄ peaks at angles around 27.3 and 45.3
20 degrees, shown in Figure 2. Due to the Zn-rich nature of the absorber layer, the presence of
21 ZnSe secondary phase has to be expected. Cu_{2-x}Se and GeSe₂ secondary phases cannot be
22 identified within the accuracy of the XRD measurements. Also note that the peaks of the
23 ternary phase Cu₂GeSe₃ overlap with the main peaks of the Cu₂ZnGeSe₄ phase completely,
24 making it impossible to distinguish these phases by XRD. To visualize the secondary phases,
25 cross-section energy dispersive X-ray spectroscopy (EDX) elemental maps of the absorber
26 were acquired in scanning transmission electron microscopy (STEM) mode, shown in Figure
27 3. The observed regions of elemental inhomogeneities are attributed to ZnSe – which seems
28 to be present in large amounts at the top surface of the absorber – and Cu₂GeSe₃ / Cu_{2-x}Se
29 phases – which are present more at the grain boundaries and at the backside Mo interface.
30 Some of the absorbers were lift-off in order to record Raman spectra near the EVAP-
31 Cu₂ZnGeSe₄/Mo interface. Both sides (front absorber and at the back side, i.e. near the back
32 contact) were analyzed. At the front Cu₂ZnGeSe₄ side (as published in [29]), only Cu₂ZnGeSe₄
33 is clearly detected, but presence of Cu₂GeSe₃ and Cu_{2-x}Se cannot be excluded as their Raman
34 peaks overlap with Cu₂ZnGeSe₄. At the back side only 2H-MoSe₂ related peaks are observed.
35 Time and energy resolved photoluminescence measurements (not shown) reveal a PL peak
36 at an energy of about 1.36 eV, with a decay time in the order of 2 ns. The band gap of this
37 absorber is thus too small to be employed as a top cell of tandem devices. However, due to

1 the high throughput of the evaporation process route/equipment, a large number of respective
2 EVAP-Cu₂ZnGeSe₄ samples are available and were thus (for practical reasons and to allow for
3 good statistics) chosen for most of our optimization efforts with respect to the absorber
4 surface treatment (see Section 2.2.1), the buffer layer (see Section 2.2.2), and the TBC (see
5 Section 2.4).

6 2.1.2. Ge-BASED COMPOUNDS BY SOLUTION-BASED PROCESS

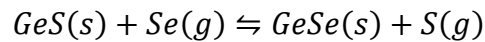
7 The SOL-Cu₂ZnGe(S,Se)₄ absorbers were deposited in a two-step process as schematically
8 drawn in Figure S3. A metal salt solution was deposited onto a Mo-coated SLG substrate by
9 doctor-blade coating with subsequent drying on a hot plate. Different solvents, metal salts
10 and chalcogen sources have been evaluated in a previous manuscript [14]. Here, the chemical
11 composition of the absorbers is Cu/(Zn+Ge)=0.7 and Zn/Ge=1.0 which is slightly more Cu-
12 poor than the EVAP-Cu₂ZnGeSe₄ layers. The chemical and electronic structure of respective
13 SOL-Cu₂ZnGe(S,Se)₄ absorbers and, in particular, the impact of the absorber formation by
14 annealing in Se-atmosphere has been monitored by lab-based soft x-ray photoelectron
15 spectroscopy (XPS) and synchrotron-based HAXPES. The XPS measurements were
16 performed in the off-synchrotron analysis chamber at EMIL in ultra-high vacuum (base
17 pressure < 5×10⁻¹⁰ mbar) employing a non-monochromatized Mg K_α (1253.56 eV) x-ray tube
18 (PREVAC RS40BI) as excitation source. The photoelectrons were detected by a Scienta
19 Omicron Argus CU electron analyzer. HAXPES was measured at beamline BL15XU at SPring-
20 8 using an excitation energy of 6 keV and a Scienta R4000 electron analyzer (see [15,16] for
21 more details on the experimental setup; same measurement conditions apply for the data
22 shown in Figure 1). Figure 4 shows the XPS S 2p/Se 3p (left panel) and HAXPES shallow core
23 level (right panel) spectra of a SOL-Cu₂ZnGe(S,Se)₄ sample prepared from a solution of Cu-,
24 Zn- and Ge-oxides in water and ammonium thioglycolate. Upon selenization, a clear Se 3d
25 signal in the shallow core level region and the Se 3p core level dominating the S 2p/Se 3p
26 energy region can be observed. The fit of the spectrum with S 2p and Se 3p doublets (see top
27 spectrum in Figure 4 – left panel) reveals the presence of at least two Se species, and two S
28 species – where the secondary (S) peak most likely indicates the presence of S-O_x and Se-O_x
29 (with x ≥ 3). The presence of Se-O_x is also indicated by the high-binding energy shoulder of
30 the Se 3d line in the shallow core level region (and depicted in the right panel of Figure 4).
31 Quantifying the fit results yields a (surface) [S]/([S]+[Se])-ratio of approximately 0.1,
32 significantly lower than the bulk composition of 0.3 [14]. The chemical environment of S in
33 the absorber precursor layer (i.e., before selenization) is also rather complex – as indicated
34 by the broad S 2p spectrum with a low binding energy shoulder (in the bottom spectrum in
35 Figure 4 – left panel), which significantly deviates from the expected spectral shape of a S 2p
36 doublet (see blue fit component on the top spectrum). The shallow core level photoemission
37 lines additionally reveal that the selenization process impacts the Zn/Cu ratio (the Cu 3p line

1 intensity is significantly increased) and the chemical bonding environment of Ge (see inset of
2 Figure 4 – right panel). Presumably, oxidized Ge is converted to form Ge-Se bonds upon
3 selenization. Finally, the location of the valence band maximum at 0.2 (± 0.1) eV (below the
4 Fermi level), indicated by the arrow in Figure 4 (right panel), is in agreement with a p-type
5 doped material, which can generally be observed for these kinds of absorbers.

6 To fabricate solar cells, CdS buffer layers are deposited by chemical-bath deposition (CBD)
7 followed by a sputtered ZnO and ZnO:Al layer. Although the band alignment of
8 $\text{Cu}_2\text{ZnGe}(\text{S,Se})_4$ with CdS is believed to be non-ideal, in a direct comparison with potential
9 alternative buffer layer candidate materials a CdS buffer was found to result in the highest
10 efficiencies [17]. The morphology of a SOL- $\text{Cu}_2\text{ZnGe}(\text{S,Se})_4$ absorber with CdS buffer can be
11 seen in the cross-section transmission electron microscopy (TEM) image displayed in Figure
12 S4(a). It shows two distinct layers within the SOL- $\text{Cu}_2\text{ZnGe}(\text{S,Se})_4$: larger grains on top and
13 smaller grains at the bottom. Note that the CdS layer on top of the absorber is only 50 nm
14 thick and therefore hard to identify in this image. All elements are for the most part
15 homogeneously distributed within the absorber layer; therefore, only the distribution of Zn
16 signal is shown in Figure S4(b), where some brighter spots in the large-grain layer can be seen,
17 which we interpret as indication for the presence of a $\text{Zn}(\text{S,Se})_2$ secondary phase. Additionally,
18 the signal of carbon residues that arise from thiourea is displayed in Figure S4(c). Here carbon
19 is only present in the small-grain layer, whereas the large-grain layer is mostly carbon-free.
20 With a higher magnification (not shown), an amorphous layer covering the $\text{Cu}_2\text{ZnGe}(\text{S,Se})_4$
21 particles can be seen. The distribution of Cd [Figure S4(d)] shows that, in contrast to other
22 investigations of kesterite absorbers with a CBD-processed CdS buffer [18], no major
23 diffusion of Cd into the absorber layer can be detected.

24 Our standard solution-based deposition approach results in SOL- $\text{Cu}_2\text{ZnGe}(\text{S,Se})_4$ absorber
25 material with a band gap of around 1.5 eV [14]. For application in tandem solar cells, a slightly
26 higher absorber band gap would be advantageous. One possible means to increase the band
27 gap would be a partial or complete cation substitution, e.g., Si for Ge [9], Ag for Cu [19], or
28 Ba for Zn [20]. However, a more complicated phase diagram is expected when using
29 additional elements, and so we focus on increasing the band gap by tuning the anion
30 composition (i.e., the $[\text{S}]/([\text{S}]+[\text{Se}])$ -ratio), a well-established method for $\text{Cu}_2\text{ZnSn}(\text{S,Se})_4$
31 absorbers. In general, the anion composition can be controlled (i) in the metal salt solution
32 and/or (ii) during the annealing process. It is used in slight excess to ensure that enough S is
33 present to form the kesterite phase during the drying step on a hot plate. If one would like
34 to lower the band gap of the SOL- $\text{Cu}_2\text{ZnGe}(\text{S,Se})_4$ absorber, thiourea could partly or
35 completely be replaced by selenourea to decrease the $[\text{S}]/([\text{S}]+[\text{Se}])$ -ratio or fabricate S-free
36 SOL- $\text{Cu}_2\text{ZnGeSe}_4$ absorbers. However, further increasing the amount of thiourea would only
37 lead to excess chalcogen that cannot be incorporated into the kesterite lattice (and also more

1 residual carbon and nitrogen) and does, therefore, not lead to an increase of the
2 $[S]/([S]+[Se])$ -ratio and thus absorber band gap. Therefore, we focus on increasing the
3 $[S]/([S]+[Se])$ -ratio during the annealing step, following approach (ii). The most obvious
4 procedure would be to anneal the sample in the simultaneous presence of Se and S. However,
5 the boiling point of S is 445°C [21], considerably lower than the annealing temperature of
6 550°C, and thereby does not allow a constant S supply during the annealing. Therefore, GeS
7 is used as an additional sulfur source [22], which is expected to release S into the gas phase
8 via the following reaction:



10 To allow for fine-tuning of the absorber band gap, the amount of GeS was varied between 0
11 and 100 mg. As a result, S is incorporated into the kesterite lattice, as can be seen from the
12 shift of the 112-reflection in the XRD patterns displayed in Figure 5. Using Vegard's law the
13 $[S]/([S]+[Se])$ -ratio can be estimated based on this data, revealing that it varies in a range
14 between 0.27 and 0.50 [22]. However, the peak shape of the 112-reflections slightly changes
15 with the amount of GeS. Starting from 40 mg (resulting in an absorber with a band gap of 1.67
16 eV [22]), a shoulder at higher diffraction angles is visible, indicating the coexistence of an
17 orthorhombic phase that is known to occur for high $[S]/([S]+[Se])$ -ratios in $Cu_2ZnGe(S,Se)_4$
18 absorbers [23].

19 To evaluate the influence on the solar cell performance, the current density-voltage [i.e., $J(V)$]
20 characteristics of the best solar cells from SOL- $Cu_2ZnGe(S,Se)_4$ absorbers with external
21 quantum efficiency (EQE)-derived band gaps of 1.5, 1.6 and 1.7 eV (corresponding to
22 $[S]/([S]+[Se])$ -ratios of 0.27, 0.39, and 0.50, respectively) are compared in Figure 6; the
23 corresponding cell parameters are listed in Table 1. As expected, the short-circuit current
24 density (J_{sc}) decreases with increasing absorber band gap. The open circuit voltage (V_{oc})
25 increases considerably from 617 to 683 mV when the absorber band gap is increased from
26 1.5 to 1.6 eV, but decreases for the 1.7 eV absorber. The fill factor (FF) shows a slight decrease
27 with absorber band gap, and efficiency reducing from 6.0 to 2.7 %. The loss in V_{oc} for devices
28 based on absorbers with a band gap larger than 1.6 eV represents the most crucial loss in this
29 sample series, which might be linked to the above-mentioned coexistence of a kesterite and
30 an orthorhombic phase. However, the band alignment between absorber and buffer layer
31 might also become severely performance limiting, especially for solar cells based on 1.7 eV
32 band gap $Cu_2ZnGe(S,Se)_4$ absorbers. To make these absorbers viable for application as top
33 cells for tandem configurations, significant efficiency enhancements are required (see
34 discussion below). In order to achieve this improvement of wide band gap kesterite solar cell
35 efficiencies, an optimization of all layers in the TF layer stack, especially the buffer/absorber
36 interface, has to be performed (see Section 2.2).

37

2.2.SURFACE TREATMENT AND BUFFER LAYER OPTIMIZATION

For the absorber layers discussed in Section 2.1, two paths toward optimization of performance were pursued: (i) selective etching of the ZnSe secondary phases (mentioned in Section 2.1.1.2) was successfully carried out and the impact on the final solar cell properties was determined (as discussed in Section 2.2.1). (ii) The CdS buffer layer deposition was optimized, and the employment of alternative buffer layers evaluated (as discussed in Section 2.2.2). Due to its better availability this work – unless stated otherwise – was done on evaporated EVAP-Cu₂ZnGeSe₄ absorbers.

2.2.1. ABSORBER SURFACE TREATMENT

Various absorber characterizations techniques reveal the presence of ZnSe at the surface of EVAP-Cu₂ZnGeSe₄ kesterites prepared by the two-step process of evaporating metal layers in vacuum with subsequent selenization of the layer stack (detailed in Section 2.1.1.2). The presence of secondary phases at the absorber/buffer interface is usually reported to have a deleterious effect on the efficiency of the resulting solar cells [24]. To prevent this, a (selective) chemical etching process for ZnSe is included as part of the standard procedure to prepare efficient solar cells. To find the proper etching procedure, we identified two previously reported etching strategies: (i) acidic etching with hot HCl, and (ii) an oxidation route at room temperature with KMnO₄ in a sulfuric acid medium [25]. Raman spectroscopy with an excitation wavelength of 458 nm allows detection of even small traces of ZnSe due to the resonant measurement conditions (i.e., excitation energy is close to the band gap of ZnSe, ≈ 2.7 eV) [26], hence, (resonant) Raman spectroscopy was used as the main characterization tool to aid in determining the optimal experimental etching conditions (temperature, concentration, duration) that result in a ZnSe-free EVAP-Cu₂ZnGeSe₄ surface. For approach (i), this means etching with a 12 wt% HCl solution, see Figure 7. For approach (ii), a 2-minute etch at room temperature in an aqueous solution of 1 mol/L KMnO₄ in 1 mol/L H₂SO₄ is sufficient to effectively remove ZnSe. Ultimately, the HCl etching was chosen as the standard etching procedure based on practical arguments (parameter control, processing, and solution stability). The optimized HCl etching conditions used in standard solar cell manufacturing have been determined to be: 15 min etching in a 12 wt% HCl solution at a temperature of 80 °C.

Solar cells were prepared based on EVAP-Cu₂ZnGeSe₄ absorbers (from the same batch) grown on Mo coated Si(O,N)/SLG, followed by CBD of CdS buffer layer, sputtering of an i-ZnO/ZnO:Al window bi-layer and finalized by e-beam deposition of Ni/Al/Ni grids for the front contact. Two absorbers served as references (i.e., not etched) and three were HCl treated at 60, 70, and 80 °C. Resonant Raman spectra confirm that only the untreated references contain ZnSe at the surface. The effect of this etching procedure on V_{OC}, FF, and EQE are presented in Figures 8 and 9. The V_{OC} of the cells prepared with untreated references

1 are in the range of 500-550 mV, which corresponds to 45-50 % of the maximum achievable
2 V_{OC} ($V_{OC,max}$) for such an absorber band gap (i.e., PL peak at 1.36 eV). In comparison, high-
3 efficiency $Cu_2ZnSn(S,Se)_4$ solar cells typically achieve 55-60% of $V_{OC,max}$ [27]. The lower V_{OC}
4 observed here with Ge-kesterite solar cells is suspected to partially originate from a non-ideal
5 buffer/absorber interface (allowing for charge carrier recombination). The presence of ZnSe
6 on the surface of the absorber (or at the buffer/absorber interface) may explain the losses.
7 This explanation is supported by the fact that V_{OC} is significantly improved for solar cells for
8 which the EVAP- $Cu_2ZnGeSe_4$ absorber underwent prior HCl etching (resulting in a ZnSe free
9 absorber surface), reaching around 55 % of $V_{OC,max}$. Despite this significant V_{OC} improvement,
10 solar cells prepared with HCl-treated absorbers result in lower efficiencies due to a dramatic
11 FF loss and an EQE drop at longer wavelength (usually ascribed to a reduced collection length).

12 To determine the origin of the FF and collection length losses after HCl etching, surface
13 characterization by HAXPES has been performed at the HiKE endstation [15] equipped with
14 a Scienta R4000 electron analyzer and located at the BESSY II KMC-I beamline [16] at HZB,
15 using an excitation energy of 2.1 keV. The HAXPES survey spectra of an as-deposited (i.e.,
16 not etched; black spectrum) and a HCl etched EVAP- $Cu_2ZnGeSe_4$ sample (red spectrum) are
17 shown in Figure 10. All $Cu_2ZnGeSe_4$ -related photoemission and Auger lines can be observed,
18 as expected. In addition, signals related to oxygen (O 1s), carbon (C 1s), and for the as-
19 deposited EVAP- $Cu_2ZnGeSe_4$ also cadmium (Cd 3d) can be observed. The presence of oxygen
20 and carbon can be attributed to a surface contamination layer formed due to the (short) air
21 exposure of the samples. The significant increase of the C 1s line upon HCl etching is most
22 likely related to additional contamination during the etching procedure. The presence of
23 cadmium on the as-deposited sample is ascribed to cross contamination from CdS/EVAP-
24 $Cu_2ZnGeSe_4$ samples that have been transported in the same sample box. Due to these varied
25 and significant states of surface contamination, we deliberately refrain from attempting to
26 quantify the HAXPES data but rather discuss them qualitatively. The HAXPES survey spectrum
27 of the as-deposited EVAP- $Cu_2ZnGeSe_4$ sample is dominated by Zn and Se signals. Upon HCl
28 etching, the Zn- and Se-related signals are significantly reduced, and the Cu/Zn ratio is
29 enhanced, in good agreement with the Raman results discussed above, i.e. the presence of a
30 ZnSe (surface) phase before etching and its removal upon HCl-treatment. The inset of Figure
31 10 shows the related detail spectra of the Se $3d_{3/2}$ and $3d_{5/2}$ spin-orbit split doublet, having a
32 separation between 0.8 and 0.9 eV. The spectral shape of the Se 3d line significantly changes
33 upon HCl etching. For the HCl-etched EVAP- $Cu_2ZnGeSe_4$ sample, the peak shape is
34 attributed to the presence of (at least) two species. The main species (indicated with "M" in
35 the inset; also dominating the spectrum of the as-deposited EVAP- $Cu_2ZnGeSe_4$ sample) is
36 ascribed to a selenide, i.e., to selenium in a $Cu_2ZnGeSe_4$ and/or ZnSe environment – based
37 on the comparison of the Se 3d data with Ref. [12]. Based on this data it is not possible to
38 unambiguously differentiate between ZnSe and $Cu_2ZnGeSe_4$. The low-intensity secondary

1 species (indicated with “S” in the inset) that is responsible for the additional high-binding
2 energy spectral intensity can most likely be explained by oxidized selenium (SeO_x , $x \geq 3$).
3 However, note that due to the large spread of binding energy values found in published
4 references [12], the presence of a germanium selenide binary phase (with Ge being in an
5 oxidation state $> 2+$) and/or formation of Se-C bonds (in-line with the increased C signal) can
6 also not be ruled out as an explanation for the high-binding energy Se 3d contribution.
7 Whether and how this second Se species affects the chemical environment of additional
8 $\text{Cu}_2\text{ZnGeSe}_4$ elements and/or the electronic structure of the absorber and how this is related
9 to the observed solar cell characteristics is the topic of ongoing research. Work on the device
10 level is in progress with the goal of developing a wet-chemical treatment to remove the HCl-
11 etch induced formation of the second Se species in order to recover the FF and collection
12 length, while keeping the V_{OC} gain resulting from HCl etching.

13 2.2.2. BUFFER LAYER DEVELOPMENT

14 The most widely used buffer layer for Cu chalcogenide thin film solar cells is CdS prepared
15 by CBD. This preparation process results in a highly defect-rich material, also containing
16 oxygen (OH) and carbon impurities [28]. Some of the properties of CBD-grown CdS (e.g.
17 composition, defect nature, structure) depend on the experimental deposition parameters
18 (concentration of the precursors, temperature of the chemical bath, etc.). Consequently, the
19 CBD-CdS recipe needs to be adjusted for each absorber material for optimal solar cell
20 performance. Hence, we empirically tuned the experimental parameters of the CdS
21 deposition on the evaporated EVAP- $\text{Cu}_2\text{ZnGeSe}_4$ absorbers. We observe a V_{OC} increase with
22 increasing deposition duration, accompanied with a decrease of FF and J_{SC} after a critical
23 duration. More details about the buffer layer optimization, which resulted in a new record
24 efficiency of 7.6 % for $\text{Cu}_2\text{ZnGeSe}_4$ based solar cells, can be found in Ref. [29].

25 Although it is the most-used buffer material for kesterite solar cells, CdS has a quite low
26 optical band gap energy (2.4 eV) and high absorption coefficient for a material that would
27 ideally be transparent. Consequently, there is a loss in current due to absorption of solar
28 radiation in the CdS is in the range of 1-2 mA/cm². In case of a potential kesterite/Si tandem
29 configuration, this loss would manifest in a 4 to 14 % relative decrease of the theoretically
30 achievable J_{SC} [3]. Moreover, another important prerequisite to reach high efficiency is an ideal
31 buffer/absorber interface that allows for lossless charge carrier transport without barriers for
32 charge carriers and preventing high-rate charge carrier recombination routes. In order to
33 systematically optimize the buffer/kesterite interface, we prepared solar cells based on wet-
34 chemical deposited (see Section 2.1.2) 1.5 (+/- 0.05) eV band gap SOL- $\text{Cu}_2\text{ZnGe}(\text{S},\text{Se})_4$
35 absorbers (prepared according to the solution approach discussed in detail in Section 2.1.2)
36 and different buffer layer materials. The five different buffer materials used were: sputtered
37 (“rf”) $\text{Zn}(\text{O}_{0.6},\text{S}_{0.4})$, CBD- $\text{Zn}(\text{O},\text{S})$, CBD-CdS, atomic layer chemical vapor deposited (ALCVD)

1 In_2S_3 , and co-evaporated (“co-evap.”) CdIn_2S_4 . A detailed discussion can be found in Ref. [17],
2 briefly: Compared to the CdS reference, In_2S_3 and $\text{Zn}(\text{O}_{0.6}\text{S}_{0.4})$ buffers have a higher
3 transmission, i.e., less absorption in the buffer layer (in the 350-500 nm wavelength range), as
4 shown in Figure II. Solar cells with $\text{Zn}(\text{O}_{0.6}\text{S}_{0.4})$ buffers also yield higher V_{OC} values. For these
5 devices, a higher activation energy of the dominant recombination process was also derived
6 (compared to the CdS reference) [17], strongly suggesting a more preferable electronic
7 structure of the buffer/SOL- $\text{Cu}_2\text{ZnGe}(\text{S},\text{Se})_4$ interface. The sputtered- $\text{Zn}(\text{O}_{0.6}\text{S}_{0.4})$ buffered
8 solar cells, however, achieve a lower overall efficiency, mainly due to reduced FF and J_{SC} , as
9 presented in Table SI [17]. We speculate that those losses originate from the nature of the
10 deposition method, as all vacuum deposited buffer layers suffer from similar J_{SC} and FF losses,
11 compared to solution-prepared CdS. For that reason, we also investigated wet-chemically
12 deposited Zn(O,S) buffers. With CBD-Zn(O,S) buffers, SOL- $\text{Cu}_2\text{ZnGe}(\text{S},\text{Se})_4$ based solar cells
13 achieve similar FF and J_{SC} values as the CdS reference, but lower V_{OC} values. A tentative
14 explanation for this observation is the different composition of CBD-Zn(O,S) and sputtered-
15 $\text{Zn}(\text{O}_{0.6}\text{S}_{0.4})$ buffers: certainly the O/S ratio, which determines the optical band gap of the
16 Zn(O,S) material, can be different and the CBD-Zn(O,S) buffer may also contain oxide,
17 hydroxide (OH), and/or carbon impurities, which can also have an impact on the
18 optoelectronic properties. Additional work is in progress to optimize the CBD-Zn(O,S) buffer
19 aiming at combining the good J_{SC} and FF values with the high V_{OC} that is obtained when
20 sputtered- $\text{Zn}(\text{O}_{0.6}\text{S}_{0.4})$ is used as a buffer.

21

22 2.3.DEVICE SIMULATIONS

23 Numerical simulations were carried out using the SCAPS software [30] to determine the best
24 device design for $\text{Cu}_2\text{ZnGe}(\text{S},\text{Se})_4$ -based top cells in a tandem configuration, with a focus on
25 suggesting suitable TBCs. The parameters used in the simulations are listed in Table S2
26 [31,32]. Most of the parameters related to the absorber material, such as thickness, doping
27 concentration, band gap, and absorption coefficient, were extracted from (our own) electrical
28 and optical measurements. Parameters related to MoSe_2 and MoO_3 were taken from
29 literature, and those related to CdS and ZnO:Al layers are already available in the SCAPS
30 software. Two configurations were tested in the simulations: $\text{Cu}_2\text{ZnGe}(\text{S},\text{Se})_4$ substrate or
31 superstrate solar cells, as shown in Figure S5. In the standard configuration [substrate, Figure
32 S5(a)], a thin layer of MoSe_2 was inserted in the model between the $\text{Cu}_2\text{ZnGe}(\text{S},\text{Se})_4$ absorber
33 layer and the Mo contact. The presence of MoSe_2 layer at the absorber/Mo interface was
34 previously reported for $\text{Cu}(\text{In},\text{Ga})\text{Se}_2$ [33] and $\text{Cu}_2\text{ZnSnSe}_4$ [34] TF solar cells. It was shown
35 to be beneficial for TF solar cells performance if its thickness is controlled to avoid detrimental
36 effects on series resistance. The improvement of the solar cell performance is mainly due to
37 a reduction of the barrier height and better charge carrier collection at the interface between

1 the absorber and the Mo contact if MoSe₂ is present. For tandem cells, the Mo back contact
2 needs to be replaced by a TBC, see Figure S5(b). However, most of the transparent
3 conductive oxides (TCOs) used in solar cells have a low work function (4.7-4.9 eV [35]) and
4 thus – if Anderson’s rule holds true for these complex heterojunctions – may not result in a
5 preferable energy level alignment with the Cu₂ZnGe(S,Se)₄ absorber layer when used as back
6 contact. In this case, the use of an intermediate layer, such as a thin MoSe₂ or MoO₃, can
7 mitigate this issue. MoO_x was successfully used in superstrate configuration as an interfacial
8 layer between a transparent SnO₂:In (ITO) back contact and Cu(In,Ga)Se₂ absorbers [36] and
9 was shown to also be a good interfacial layer for the Cu₂ZnSnSe₄ based solar cells (applied
10 either as a layer between the absorber and the Mo contact to improve the back contact
11 properties or as a primary back contact) [37-38].

12 Figure S6 shows the J(V) curves calculated for different device configurations. The solar cell
13 parameters are given in Table 2. For the Cu₂ZnGe(S,Se)₄ substrate configuration (a), the
14 calculated J(V) curve is based on series resistance and shunt resistance values of 4.7 and
15 365 Ωcm², respectively. These resistances have been extracted from the J(V) curve of one of
16 the most efficient EVAP-Cu₂ZnGeSe₄ substrate solar cells (5.4 % power conversion efficiency).
17 In the configurations (b)-(d), the J(V) curves were calculated after the (simulated) optimization
18 of the absorber doping concentration (10¹⁶ cm⁻³) and of the values for series and shunt
19 resistance ($R_s \leq 0.5 \Omega\text{cm}^2$; $R_{sh} \geq 800 \Omega\text{cm}^2$). In case of a superstrate with TBC [configuration
20 (c)], the low solar cell performance is due to a strong reduction of the V_{OC} caused by the low
21 work function of ZnO:Al (AZO). The best configuration for superstrate solar cell was
22 obtained by considering a thin “buffer layer” of MoO₃ between the absorber and a TCO back
23 contact (d). It should be noticed that an ITO back contact acts also as a Na barrier. If
24 insufficient Na content limits the device performance, however, Na needs to be deliberately
25 added in a controlled way, e.g. by means of post-deposition treatment [39].

27 2.4. TRANSPARENT BACK CONTACTS

28 TBCs for potential use in the wide band gap Cu₂ZnGe(S,Se)₄ kesterite top cell of a four
29 terminal photovoltaic tandem cell with a c-Si bottom cell have been studied. In addition to
30 the electronic structure considerations in the previous section, the back contact must be
31 transparent for photons with an energy below the band gap of the absorber layer and stable
32 under its processing conditions. Independent of the processing route [evaporation-based (see
33 Section 2.1.1) or solution-based (see Section 2.1.2.)], the kesterite absorber is formed by high-
34 temperature annealing of the precursor layer stack in H₂Se and/or H₂S atmosphere. It is
35 expected that this selenization/sulfurization will be the most critical processing step that the
36 TBC has to withstand. H₂Se is a more powerful reducing agent than is H₂S [40], and so we
37 focus on the impact of annealing in H₂Se atmosphere on the optoelectronic and chemical

1 properties of the TBCs in the following. The most widely used TCOs: ITO, AZO, and SnO₂:F
2 (FTO) – were selected for exposure tests [41,42]. It is assumed that the S-containing
3 atmosphere during annealing required to achieve the $[S]/([S]+[Se])$ composition necessary for
4 the desired higher absorber band gap will have similar effects.

5 In order to simulate the impact of H₂Se exposure during a Cu₂ZnGe(S,Se)₄ deposition process,
6 the optical and chemical properties of the selected TCOs have been tested before and after
7 exposure to a 20 sccm H₂Se flow for 15 min at various treatment temperatures (400 and
8 450 °C). A first screening showed that ITO had the highest likelihood for yielding working
9 devices but would require a protective top layer (to make it more stable during absorber
10 processing). Furthermore, our SCAPS simulations (see Section 2.3) of Cu₂ZnSn(S,Se)₄ devices
11 had shown that employing ITO instead of Mo (which is the standard back contact for single-
12 junction devices) would result in an efficiency drop of 60 rel.% (see Table 2). The same
13 simulations showed that this deterioration may be fully prevented by using an additional MoO₃
14 interlayer between ITO and absorber resulting even in an efficiency gain of 80 rel.% (see Table
15 2). Hence, thin sputtered MoO₃ layers applied on top of a 135-nm-thick sputtered ITO before
16 absorber deposition – as protection layer and for improved energy level alignment – were
17 first explored. However, MoO₃ is significantly reduced upon H₂Se exposure; in Section 2.4.1,
18 we explore alternative protective layers.

19 2.4.1. PROTECTIVE TOP LAYERS

20 In this section, the effectiveness of Al₂O₃, InZnO_x (IZO), and TiO₂ as protection of ITO during
21 selenization/sulfurization is explored. The study is conducted by means of H₂Se exposure tests
22 at 400°C and 450°C (i.e., annealing temperatures relevant for absorber formation), as well as
23 by experiments on the device level. The top layers were deposited by means of atmospheric
24 pressure spatial atomic layer deposition (S-ALD, plasma enhanced for IZO) [43].

25 2.4.1.1. LAYER PROPERTIES

26 Al₂O₃ is known to be an excellent passivation and barrier (i.e., protective layer) material of
27 high chemical stability; it is however electrically insulating. IZO and TiO₂ are candidates for
28 forming more conductive protective layers. In order to determine the minimum thickness for
29 being a sufficient protective top layer and to test if such a thickness would yield a working
30 device, a set of Al₂O₃ (1-30 nm), IZO (1-120 nm), and TiO₂ (2-60 nm) layers of different
31 thicknesses were deposited by means of S-ALD on ITO coated SLG substrates. The
32 absorption spectra (derived from reflectance and transmittance) shown in Figure 12 suggest
33 that the decrease of ITO transmittance (i.e., increase of absorption) induced by H₂Se exposure
34 could (to some degree) be prevented with a > 2 nm Al₂O₃ (not shown), > 30 nm IZO, or >
35 60 nm TiO₂ top layer. However, the TiO₂ layers are less effective at temperatures of 450°C
36 and higher [see Figure 12(c)]. After H₂Se exposure at 450°C, the average absorption for an

1 135-nm-thick ITO layer with a 30-nm-thick IZO and 60-nm-thick TiO₂ protective layer is 8
2 and 18 %, respectively, in the near infra-red regime (between 750 nm and 1100 nm).

3 HAXPES was used for chemical structure analysis of the IZO/ITO back contact configuration
4 and its changes upon H₂Se exposure in order to probe the deterioration of ITO and the
5 protection mechanism of IZO. Note that same measurement conditions apply as for the
6 HAXPES data shown in Figures 1 and 4. The Sn 3d XPS spectra of a bare ITO sample and ITO
7 samples with either a 10 or a 30 nm protective IZO top layer before and after H₂Se treatment
8 at 450 °C are shown in Figure 13. Before the H₂Se treatment, for the bare ITO and 10 nm
9 IZO/ITO sample, Sn resides in a chemical environment best described by a combination of
10 ITO, SnO, and SnO₂. However, note that asymmetric core level lines are generally found for
11 (highly conductive) ITO and are generally attributed to final-state effects [44]. No Sn signal is
12 observed for the 30 nm IZO/ITO sample, due to insufficient probing depth and complete
13 coverage of the ITO by the IZO. (The inelastic mean free path of the Sn 3d photoelectrons
14 excited with 6 keV photons in In₂O₃ is around 7 nm [45]). After H₂Se treatment, the spectral
15 intensity of the Sn 3d line is significantly redistributed, indicating that the chemical
16 environment of Sn has changed; SnSe and/or SnSeO_x are likely present. Furthermore, the Sn
17 3d intensity increases after the H₂Se treatment for the 10 nm IZO/ITO sample, suggesting
18 either that Sn diffuses into the IZO layer and/or the degree of ITO coverage decreases. If the
19 protective layer does not completely cover the ITO, it will not prevent the chemical reaction
20 between ITO and H₂Se, the evidence of which is the formation of Sn-Se bonds. Additional
21 HAXPES data suggest a significant chemical interaction between IZO and H₂Se, implying that
22 IZO acts as a sacrificial agent to protect ITO from H₂Se. Note that additional measurements
23 on TiO₂/ITO test structures (not shown) reveal a different protection mechanism: TiO₂ is
24 largely unaffected by H₂Se annealing.

25 2.4.1.2. SOLAR CELL DEVICES

26 EVAP-Cu₂ZnGeSe₄-based devices were manufactured on sputtered ITO/SLG substrates with
27 S-ALD deposited Al₂O₃, IZO, and TiO₂ protective layers. As references, similarly prepared
28 devices with a standard Mo back contact on a Si(O,N)/SLG substrate were also fabricated and
29 tested. A CBD-CdS buffer and a sputtered i-ZnO/AZO bi-layer emitter was used as the front
30 window. The (5×5 cm²) EVAP-Cu₂ZnGeSe₄ cell stack samples were finished by applying a
31 Ni/Ag grid for local J(V) measurements. Table 3 depicts measured J(V) parameters of the
32 champion cells. As stated earlier, an Al₂O₃ thickness above 2 nm is needed for an effective
33 H₂Se protection of ITO. However, the 3 nm thick Al₂O₃ layer used here already reduces the
34 cell performance dramatically due to its insufficient conductivity. This issue could be
35 overcome by using a perforated Al₂O₃ layer, which (through the formed point contacts) allows
36 sufficient charge carrier transport while also acting as a passivation and barrier layer. Devices
37 with an ITO back contact with or without either a 30 nm TiO₂ or IZO protective top layer

1 function better, yielding efficiencies of about 85-90 % of that of reference cells with a Mo back
2 electrode. The lower efficiencies likely result from a higher sheet resistance of the back
3 contact and a presumably less ideal energy level alignment at the absorber/back contact
4 interface compared to the Mo back electrode. The combination of ITO back electrode with
5 TiO_2 protection layer results in a higher V_{OC} than an ITO back electrode with or without IZO
6 protection layer, but not in a higher J_{SC} value – finding an explanation for this observation is a
7 subject of ongoing discussion.

8 Figure 14 depicts the absorption (derived from reflectance and transmittance) for a complete
9 EVAP- $\text{Cu}_2\text{ZnGeSe}_4$ solar cell layer stack on a 60 nm TiO_2 protected ITO back electrode. The
10 absorption of the complete cell stack for energies directly below E_{G} ($\text{Cu}_2\text{ZnGeSe}_4$) is 65 % for
11 60 nm TiO_2 /ITO and 55 % for 30 nm IZO/ITO (not shown) back contacts. These values are
12 higher than the sum computed from the absorption of the individual layers (i.e., back contact
13 after H_2Se exposure, absorber, and front window), as illustrated in Figure 14 for the 60 nm
14 TiO_2 /ITO back contact. This may be due to slightly varying absorber layer deposition and/or
15 selenization process conditions, annealing-induced formation of species at the absorber
16 (precursor)/TBC interface, or internal reflections and higher absorption of the front window
17 when deposited on the actual (rough) absorber layer. In order to reduce the optical losses in
18 a complete device, more analysis of the composition and morphology of the layers and their
19 interfaces in the cell stack will be needed. To reduce near-infrared absorption due to free
20 charge carriers in both the highly-doped back and front contact, more effort is required to
21 develop transparent materials with high mobilities and reasonable charge carrier densities.

22 23 3. OUTLOOK

24 The bottom cell in a tandem configuration will only receive the illumination transmitted
25 through the top cell, and so a good transmission at $h\nu <$ than the top cell absorber band gap
26 is crucial for the top cell structure to successfully be employed in tandem configurations, as
27 discussed in the previous section. A thin top cell combined with a TBC is generally used to
28 assure this. To investigate the effect of the top cell transparency on the performance of the
29 bottom cell (c-Si), we calculated the efficiency of the bottom cell as a function of the light
30 transmitted through the top cell, as shown in Figure 15. The bottom cell is modeled as a 25
31 % efficient silicon cell with rear locally diffused contacts (PERL technology [46]) and
32 Lambertian light trapping [47-48]. For the tandem cell, a four-terminal mechanically stacked
33 configuration is considered. In Figure 15, the efficiency of the c-Si bottom cell under the
34 absorbing 1.5 eV band gap $\text{Cu}_2\text{ZnGe}(\text{S},\text{Se})_4$ -based cell is shown as a function of top cell
35 transmission. Furthermore, the total efficiency of the tandem configuration assuming a top
36 cell efficiency of 8, 15, and 22 % is shown. In the case of a $\text{Cu}_2\text{ZnGe}(\text{S},\text{Se})_4(1.5 \text{ eV})$ -based top

1 cell of 8 % efficiency (i.e., a performance level similar to the one reached as a result of joint
2 research efforts of this consortium, see Section 2.2.2), a transparency higher than 80 % is
3 required to achieve a total tandem device efficiency that is higher than the efficiency of the c-
4 Si bottom cell alone (25 %, horizontal dashed line in Fig. 21). In case the efficiency of the top
5 cell can be increased to 15 % (a performance level that seems feasible based on our device
6 simulation in Section 2.3, see Table 2), a transparency above 50 % is sufficient for viable
7 tandem application. Finally, for a 22 % efficient top cell (a performance level that has been
8 shown for other polycrystalline chalcogenide-based absorbers [2]) respective tandem devices
9 would reach efficiencies > 25% with even more relaxed top cell transparency requirements.

10 A maximal transparency of approximately 40 % for a real-world $\text{Cu}_2\text{ZnGe}(\text{S},\text{Se})_4/\text{TBC}$ layer
11 stack was shown in this contribution (see Fig. 20 and discussion in Section 2.4.1.2); there is a
12 realistic potential to increase this to 60 % if chemical reactions at the interfaces and/or internal
13 reflections can be minimized. Hence, wide band gap kesterites might very well represent a
14 material class that may be used as absorber in tandem device top cells if further significant
15 advancements in cell performance (8 → 15%) and transmission (40 → 60%) are achieved.
16 Based on the progress presented in this paper (compare status 2015 and 2018 indicated as
17 ❶ and ❷ in Figure 15), it indeed seems feasible to reach the realistic performance scenario
18 (❸ in Figure 15) if optimization efforts continue.

20 4. CONCLUSIONS

21 Absorbers in which Sn had been substituted by Si did not result in functioning solar cells; most
22 likely due to too high doping (in the order of 10^{18} cm^{-3}) and/or the formation of SiO_2 at the
23 absorber surface. However, $\text{Cu}_2\text{ZnGe}(\text{S},\text{Se})_4$ absorbers with band gaps above 1.5 eV have
24 been successfully developed and integrated into solar cells. Typically, ZnSe is present in large
25 amounts on the top surface of these absorbers; it is shown here that this impurity can be
26 selectively removed with chemical etching: (i) with 12 wt% HCl at a temperature of 60-85 °C,
27 and (ii) in 1M KMnO_4 / 1M H_2SO_4 aqueous solution. The standard CBD-CdS has been
28 optimized, resulting in a record efficiency of 7.6 % for EVAP- $\text{Cu}_2\text{ZnGeSe}_4$ based solar cells
29 (with Mo back contact). In_2S_3 , $\text{Zn}(\text{O},\text{S})$, and CdIn_2S_4 alternative buffer layers were also tested,
30 where the highest V_{OC} and presumably the best electronic buffer/absorber interface structure
31 could be obtained with sputtered $\text{Zn}(\text{O},\text{S})$.

32 The solar cell performance of substrate/superstrate $\text{Cu}_2\text{ZnGe}(\text{S},\text{Se})_4$ solar cells with TBC for
33 tandem application was simulated using SCAPS to evaluate various configurations and identify
34 performance-limiting factors. It was found that when low work function, TCO-based, TBCs
35 (like ITO) are used, an “interlayer” is required to reduce the blocking barrier at the
36 absorber/TCO interface, ideally achieving an Ohmic contact. The device simulation suggests

1 MoO_x as an ideal interlayer candidate material for Cu₂ZnGe(S,Se)₄ superstrate cells for
2 tandem applications. MoO_x is, however, unstable under real-world absorber processing
3 conditions; the use of an alternative, stable material causes the majority of respective
4 (transparent) cells to be still limited by a low V_{OC}.

5 ITO was shown to be a well-performing candidate for a TBC, but it requires a protective top
6 layer (i.e., Al₂O₃, IZO, or TiO₂) if it is to remain transparent after exposure to the Se (and/or
7 S) atmosphere needed for the absorber deposition process. ITO back contacts with a
8 protective layer of 30-nm-thick IZO or 60-nm-thick TiO₂ have an average absorption of 8 and
9 18 %, respectively, in the near infra-red regime. The efficiency of solar cells using an ITO with
10 IZO or TiO₂ protective layers achieves 85-90 % of the performance of reference cells with
11 Mo back contact (at a maximal transparency of 40 %).

12 In summary, Cu₂ZnGe(S,Se)₄ absorbers with potential for future application as top cell in
13 tandem configurations have been developed. Different optimization routes mostly addressing
14 the buffer/absorber interface have been suggested and proven to be effective to advance
15 device performance. In order to make wide band gap kesterites a prime candidate absorber
16 material for the top cell in tandem devices, similar approaches are crucially needed extending
17 the efforts to all aspects of the complete cell stack, tackling interface *and* bulk properties in
18 order to improve cell efficiency and transmission. In order to accomplish this challenge, it is
19 proposed to focus future research on increasing the solar cell performance before addressing
20 the transparency of these solar cell devices.

1 ACKNOWLEDGEMENTS

2 This project has received funding from the European Union's Horizon 2020 research and
3 innovation program under grant agreement N° 640868. The synchrotron radiation
4 experiments were performed at the SPring-8 beamline BL15XU with the approval of the NIMS
5 Synchrotron X-ray Station (Proposals 2016A4600, 2016B4601, and 2017A4600) and at BESSY
6 II with the approval of HZB. B. Vermang has received funding from the European Research
7 Council (ERC) under the European Union's Horizon 2020 research and innovation
8 programme (grant agreement n° 715027).

11 REFERENCES

12 [1] M.A. Green, S. Hishikawa, E.D. Dunlop, D.H. Levi, J. Hohl-Ebinger, A.W.Y. Ho-Baillie,
13 Solar cell efficiency tables (version 51), Progress in Photovoltaics: Research and Applications
14 26 (2018) 3-12. (DOI: 10.1002/pip.2978)

15 [2] Solar Frontier Achieves World Record Thin-Film Solar Cell Efficiency of 22.9 %, Solar
16 Frontier press release, http://www.solar-frontier.com/eng/news/2017/1220_press.html, last
17 accessed May 23rd 2018.

18 [3] W. Shockley, H.J. Queisser, Detailed balance limit of efficiency of p-n junction solar cells,
19 Journal of Applied Physics 32 (1961) 510-519. (DOI: 10.1063/1.1736034)

20 [4] T.P. White, N.N. Lal, K.R. Catchpole, Tandem solar cells based on high efficiency c-Si
21 bottom cells: top cell requirements for >30% efficiency, IEEE Journal of Photovoltaics 4
22 (2014) 208-214. (DOI: 10.1109/JPHOTOV.2013.2283342)

23 [5] T.K. Todorov, D.M. Bishop, Y. Seog Lee, Materials perspectives for next-generation low-
24 cost tandem solar cells, Solar Energy Materials and Solar Cells 180 (2018) 350-357. (DOI:
25 10.1016/j.solmat.2017.07.033)

26 [6] S. Siebentritt, S. Schorr, Kesterites – a challenging material for solar cells, Progress in
27 Photovoltaics: Research and Applications 20 (2012) 512-519. (DOI: 10.1002/pip.2156)

28 [7] W. Wang, M.T. Winkler, O. Gunawan, T. Gokmen, T.K. Todorov, Y. Zhu, D.B. Mitzi,
29 Device characteristics of CZTSSe thin-film solar cells with 12.6% efficiency”, Advanced
30 Energy Materials 4 (2014) 1301465. (DOI: 10.1002/aenm.201301465)

31 [8] M. León, S. Levchenko, R. Serna, G. Gurieva, A. Nateprov, J.M. Merino, E. J. Friedrich, U.
32 Fillat, S. Schorr, E. Arushanov, Optical constants of Cu₂ZnGeS₄ bulk crystals, Journal of
33 Applied Physics 108 (2010) 093502. (DOI: 10.1063/1.3500439)

- 1 [9] Q. Shu, J.-H. Yang, S. Chen, B. Huang, H. Xiang, X.-G. Gong, S.-H. Wei, $\text{Cu}_2\text{Zn}(\text{Sn},\text{Ge})\text{Se}_4$
2 and $\text{Cu}_2\text{Zn}(\text{Sn},\text{Si})\text{Se}_4$ alloys as photovoltaic materials: Structural and electronic properties,
3 *Physical Review B* 87 (2013) 115208. (DOI: 10.1103/PhysRevB.87.115208)
- 4 [10] G. Brammertz, B. Vermang, H. Elanzeery, S. Sahayaraj, S. Ranjbar, M. Meuris, J.
5 Poortmans, Fabrication and characterization of ternary Cu_8SiS_6 and Cu_8SiSe_6 thin film layers
6 for optoelectronic applications, *Thin Solid Films* 616 (2016) 649-654. (DOI:
7 10.1016/j.tsf.2016.09.049)
- 8 [11] G. Brammertz, B. Vermang, H. Elanzeery, S. Sahayaraj, S. Ranjbar, M. Meuris, J.
9 Poortmans, Fabrication of ternary and quaternary chalcogenide compounds based on Cu,
10 Zn, Sn and Si for thin film photovoltaic applications, *Physica Status Solidi C* 14 (2017)
11 1600162. (DOI: 10.1002/pssc.201600162)
- 12 [12] NIST X-ray Photoelectron Spectroscopy Database, version 3.5, National Institute of
13 Standards and Technology, Gaithersburg, 2003, <https://srdata.nist.gov/xps/>, last accessed
14 May 23rd 2018.
- 15 [13] G. Brammertz, B. Vermang, M. Meuris, J. Poortmans, Crystallization properties of
16 $\text{Cu}_2\text{ZnGeSe}_4$, *Thin Solid Films* 670 (2019) 76-79 (DOI: 10.1016/j.tsf.2018.12.015).
- 17 [14] T. Schnabel, M. Seboui, E. Ahlswede, Evaluation of different metal salt solutions for the
18 preparation of solar cells with wide-gap $\text{Cu}_2\text{ZnGeS}_x\text{Se}_{4-x}$ absorbers, *RSC Advances* 7 (2016)
19 26-30. (DOI: 10.1039/C6RA23068G)
- 20 [15] S. Ueda, Y. Katsuya, M. Tanaka, H. Yoshikawa, Y. Yamashita, S. Ishimaru, Y. Matsushita,
21 K. Kobayashi, Present status of the NIMS contract beamline BL15XU at SPring-8, AIP
22 Conference Proceedings 1234 (2010) 403-406. (DOI: 0.1063/1.3463225)
- 23 [16] S. Ueda, Application of hard X-Ray photoelectron spectroscopy to electronic structure
24 measurements for various functional materials, *J. Electron Spectrosc. Relat. Phenom.* 190
25 Part B (2013) 235-241. (DOI: 10.1016/j.elspec.2013.01.009)
- 26 [17] T. Schnabel, M. Seboui, L. Choubrac, L. Arzel, S. Harel, N. Barreau, E. Ahlswede,
27 Evaluation of different buffer materials for solar cells with wide-gap $\text{Cu}_2\text{ZnGeS}_x\text{Se}_{4-x}$
28 absorbers. *RSC Advances* 7 (2017) 40105-40110. (DOI: 10.1039/C7RA06438A)
- 29 [18] M. Werner, D. Keller, S.G. Haass, C. Gretener, B. Bissig, P. Fuchs, F. La Mattina, R.
30 Erni, Y.E. Romanyuk, A.N. Tiwari, Enhanced carrier collection from CdS passivated grains in
31 solution-processed $\text{Cu}_2\text{ZnSn}(\text{S},\text{Se})_4$ solar cells, *ACS Applied Materials & Interfaces* 7 (2015)
32 12141-12146. (DOI: 10.1021/acsami.5b02435)
- 33 [19] T. Gershon, K. Sardashti, O. Gunawan, R. Mankad, S. Singh, Y.S. Lee, J.A. Ott, A.
34 Kummel, R. Haight, Photovoltaic device with over 5% efficiency based on an n-type

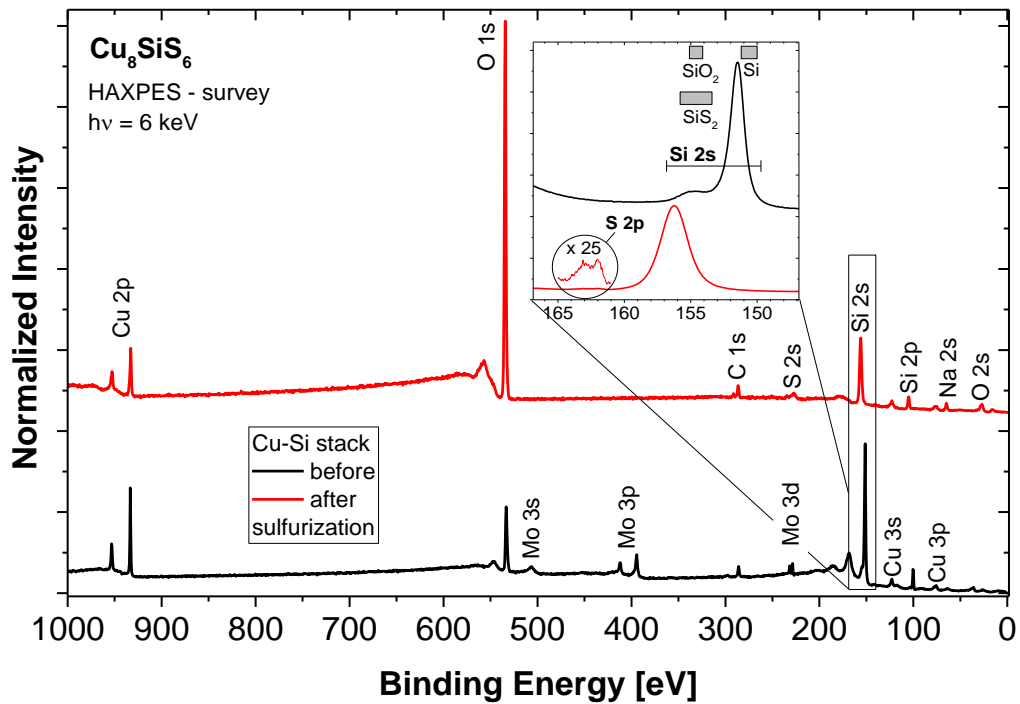
- 1 Ag₂ZnSnSe₄ absorber. *Advanced Energy Materials* 6 (2016) 1601182. (DOI:
2 10.1002/aenm.201601182)
- 3 [20] J. Ge, Y. Yu, Y. Yan, Earth-abundant orthorhombic BaCu₂Sn(Se_xS_{1-x})₄ (x = 0.83) thin film
4 for solar energy conversion, *ACS Energy Letters* 1 (2016) 583-588. (DOI:
5 10.1021/acsenergylett.6b00324)
- 6 [21] Y. Zhang, J.R.G. Evans, S. Yang, Corrected values for boiling points and enthalpies of
7 vaporization of elements in handbooks, *Journal of Chemical & Engineering Data* 56 (2011)
8 328-337. (DOI: 10.1021/je1011086)
- 9 [22] T. Schnabel, M. Seboui, E. Ahlswede, Band gap tuning of Cu₂ZnGeS_xSe_{4-x} absorbers for
10 thin-film solar cells, *Energies* 10 (2017) 1813. (DOI: 10.3390/en10111813)
- 11 [23] J. Chen, W. Li, C. Yan, S. Huang, X. Hao, Studies of compositional dependent
12 Cu₂Zn(Ge_xSn_{1-x})S₄ thin films prepared by sulfurizing sputtered metallic precursors, *Journal*
13 *of Alloys and Compounds* 621 (2015) 154-161. (DOI: 10.1016/j.jallcom.2014.09.097)
- 14 [24] M. Kumar, A. Dubey, N. Adhikari, S. Venkatesan, and Q. Qiao, Strategic review of
15 secondary phases, defects and defect-complexes in kesterite CZTS–Se solar cells, *Energy &*
16 *Environmental Science* 8 (2015) 3134-3159. (DOI: 10.1039/C5EE02153G)
- 17 [25] E.M. Gavrishchuk, E.Y. Vilkovala, O.V. Timofeev, U.P. Borovskikh, E.L. Tikhonova, Etching
18 behavior of CVD zinc selenide in inorganic acid solutions, *Inorganic Materials* 43 (2007) 579-
19 583. (DOI: 10.1134/S0020168507060039)
- 20 [26] S. López-Marino, Y. Sánchez, M. Placidi, A. Fairbrother, M. Espindola-Rodríguez, X.
21 Fontané, V. Izquierdo-Roca, J. López-García, L. Calvo-Barrio, A. Pérez-Rodríguez, E.
22 Saucedo, ZnSe etching of Zn-rich Cu₂ZnSnSe₄: an oxidation route for improved solar-cell
23 efficiency, *Chemistry: A European Journal* 19 (2013) 14814-14822. (DOI:
24 10.1002/chem.201302589)
- 25 [27] S. Bourdais, C. Choné, B. Delatouche, A. Jacob, G. Larramona, C. Moisan, A. Lafond, F.
26 Donatini, G. Rey, S. Siebentritt, A. Walsh, G. Dennler, Is the Cu/Zn disorder the main
27 culprit for the voltage deficit in kesterite solar cells?, *Advanced Energy Materials* 6 (2016)
28 1502276. (DOI: 10.1002/aenm.201502276)
- 29 [28] P. O'Brien, J. McAleese, Developing an understanding of the processes controlling the
30 chemical bath deposition of ZnS and CdS, *Journal Of Materials Chemistry* 8 (1998) 2309-
31 2314. (DOI: 10.1039/A804692A)
- 32 [29] L. Choubrac, G. Brammertz, N. Barreau, L. Arzel, S. Harel, M. Meuris, B. Vermang,
33 7.6% CZGSe solar cells thanks to optimized CdS chemical bath deposition, *Physica Status*
34 *Solidi A* (2018) Early View. (DOI: 10.1002/pssa.201800043)

- 1 [30] M. Burgelman, K. Decock, S. Khelifi, A. Abass, Advanced electrical simulation of thin
2 film solar cells, *Thin Solid Films* 535 (2013) 296-301. (DOI: 10.1016/j.tsf.2012.10.032)
- 3 [31] A. Jäger-Waldau, M.Ch. Lux-Steiner, R. Jäger-Waldau, E. Bucher, Optical and electronic
4 properties of MoSe₂ thin films prepared by soft selenization, *Spinger Proceedings in Physics,*
5 *Polycrystalline Semiconductors II* 54 (1991) 397-402. (DOI: 10.1007/978-3-642-76385-4_57)
- 6 [32] H. Simchi, B.E. McCandless, T. Meng, J.H. Boyle, W.N. Shafarman, Characterization of
7 reactively sputtered molybdenum oxide films for solar cell application, *Journal of Applied*
8 *Physics* 114 (2013) 013503. (DOI: 10.1063/1.4812587)
- 9 [33] D. Abou-Ras, G. Kostorz, D. Bremaud, M. Kälin, F.V. Kurdeseau, A.N. Tiwari, M.
10 Döbeli, Formation and characterisation of MoSe₂ for Cu(In,Ga)Se₂ based solar cells, *Thin*
11 *Solid Films* 480-481 (2005) 433-438. (DOI: 10.1016/j.tsf.2004.11.098)
- 12 [34] B. Shin, Y. Zhu, N.A. Bojarczuk, S. J. Chey, S. Guha. Control of an interfacial MoSe₂
13 layer in Cu₂ZnSnSe₄ thin film solar cells: 8.9 % power conversion efficiency with a TiN
14 diffusion barrier, *Applied Physics Letters* 101 (2012) 053903. (DOI: 10.1063/1.4740276)
- 15 [35] A. Klein, C. Körber, A. Wachau, F. Säuberlich, Y. Gassenbauer, S.P. Harvey, D.E. Proffit,
16 T.O. Mason, Transparent conducting oxides for photovoltaics: Manipulation of fermi level,
17 work function and energy band alignment, *Materials* 3 (2010) 4892-4914. (DOI:
18 10.3390/mat3114892)
- 19 [36] H. Simchi, J.K. Larsen, K. Kim, W. Shafarman, Improved Performance of Ultrathin
20 Cu(InGa)Se₂ Solar Cells With a Backwall Superstrate Configuration, *IEEE Journal of*
21 *Photovoltaics* 4 (2014) 1630-1635. (DOI: 10.1109/JPHOTOV.2014.2345436)
- 22 [37] S. Lopez-Marino, M. Espindola-Rodriguez, Y. Sanchez, X. Alobé, F. Olivia, H. Xie, M.
23 Neuschitzer, S. Giraldo, M. Placidi, R. Caballero, V. Izquierdo-Roca, A. Pérez-Rodriguez, E.
24 Saucedo, The importance of back contact modification in Cu₂ZnSnSe₄ solar cells: The role of
25 a thin MoO₂ layer, *Nano Energy* 26 (2016) 708-721. (DOI: 10.1016/j.nanoen.2016.06.34)
- 26 [38] J. Park, J. Huang, K. Sun, Z. Ouyang, F. Liu, C. Yan, H. Sun, A. Pu, M. Green, X. Hao,
27 The effect of thermal evaporated MoO₃ intermediate layer as primary back contact for
28 kesterite Cu₂ZnSnS₄ solar cells, *Thin Solid Films*, 648 (2018) 39-45. (DOI:
29 10.1016/j.tsf.2018.01.012)
- 30 [39] D. Rudmann, A.F.d. Cunha, M. Kaelin, F. Kurdesau, H. Zogg, A.N. Tiwari, G. Bilger,
31 Efficiency enhancement of Cu(In,Ga)Se₂ solar cells due to post-deposition Na incorporation,
32 *Applied Physics Letters* 84 (2004) 1129-1131. (DOI: 10.1063/1.1646758)
- 33 [40] S. Oae, J.T. Doi, *Organic sulfur chemistry: Structure and mechanisms, Heteroatom*
34 *Chemistry* 4 (1991) 531. (ISBN: 0-8493-4739-4)

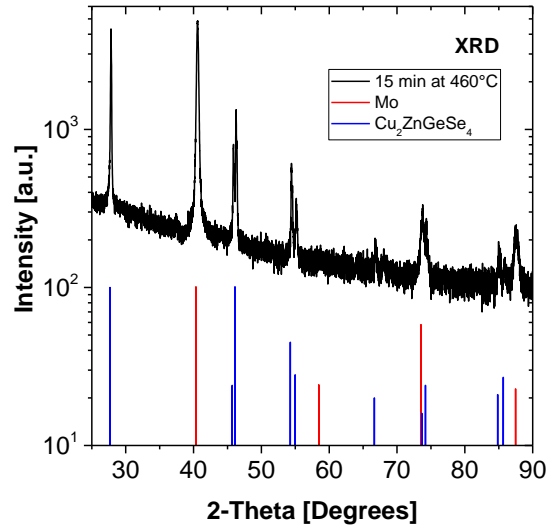
- 1 [41] I. Volintiru, A. de Graaf, J. van Deelen, P. Poodt, The influence of methanol addition
2 during the film growth of SnO₂ by atmospheric pressure chemical vapor deposition, *Thin*
3 *Solid Films* 519 (2011) 6258-6263. (DOI: 10.1016/j.tsf.2011.03.125)
- 4 [42] J. van Deelen, A. Illiberi, B. Kniknie, H. Steijvers, A. Lankhorst, P. Simons, APCVD of
5 ZnO:Al, insight and control by modeling, *Surface and Coatings Technology* 230 (2013) 239-
6 244. (DOI: 10.1016/j.surfcoat.2013.06.055)
- 7 [43] P. Poodt, D.C. Cameron, E. Dickey, S.M. George, V. Kuznetsov, G.N. Parsons, F.
8 Roozeboom, G. Sundaram, A. Vermeer, Spatial atomic layer deposition: a route towards
9 further industrialization of atomic layer deposition, *Journal of Vacuum Science and*
10 *Technology A* 30 (2012) 010802. (DOI: 10.1116/1.3670745)
- 11 [44] C. Körber, V. Krishnakumar, A. Klein, G. Panaccione, P. Torelli, A. Walsh, J.L.F. Da
12 Silva, S.-H. Wei, R.G. Egdell, D.J. Payne, Electronic structure of In₂O₃ and Sn-doped In₂O₃ by
13 hard x-ray photoemission spectroscopy, *Physical Review B* 81 (2010) 165207. (DOI:
14 10.1103/PhysRevB.81.165207)
- 15 [45] QUASES-IMFP-TPP2M Ver. 3.0 code, Inelastic electron mean free paths calculated from
16 the TPP-2M formula: S. Tanuma, C.J. Powell, D.R. Penn, Calculations of electron inelastic
17 mean free paths. V. Data for 14 organic compounds over the 50–2000 eV range, *Surface and*
18 *Interface Analysis* 21 (1994) 165-176; and H. Shinotsuka, S. Tanuma, C.J. Powell, D.R. Penn,
19 Calculations of electron inelastic mean free paths. X. Data for 41 elemental solids over the
20 50 eV to 200 keV range with the relativistic full Penn algorithm, *Surface and Interface*
21 *Analysis* 47 (2015) 871-888. (DOI: 10.1002/sia.740210302 and 10.1002/sia.5789)
- 22 [46] J. Zhao, A. Wang, P.P. Altermatt, S.R. Wenham, M.A. Green, 24% efficient PERL silicon
23 solar cell: Recent improvements in high efficiency silicon cell research, *Solar Energy*
24 *Materials and Solar Cells* 41-42 (1996) 87-99. (DOI: 10.1016/0927-0248(95)00117-4)
- 25 [47] M.A. Green, The path to 25% silicon solar cells efficiency,,: History of the silicon cell
26 evolution, *Progress in Photovoltaics: Research and Applications* 17 (2009) 183-189. (DOI:
27 10.1002/pip.892)
- 28 [48] S. Khelifi, J. Verschraegen, M. Burgelman, A. Belghachi, Numerical simulation of impurity
29 photovoltaic effect in silicon solar cells, *Renewable Energy* 33 (2008) 293-298. (DOI:
30 10.1016/j.renene.2007.05.027)

31

32

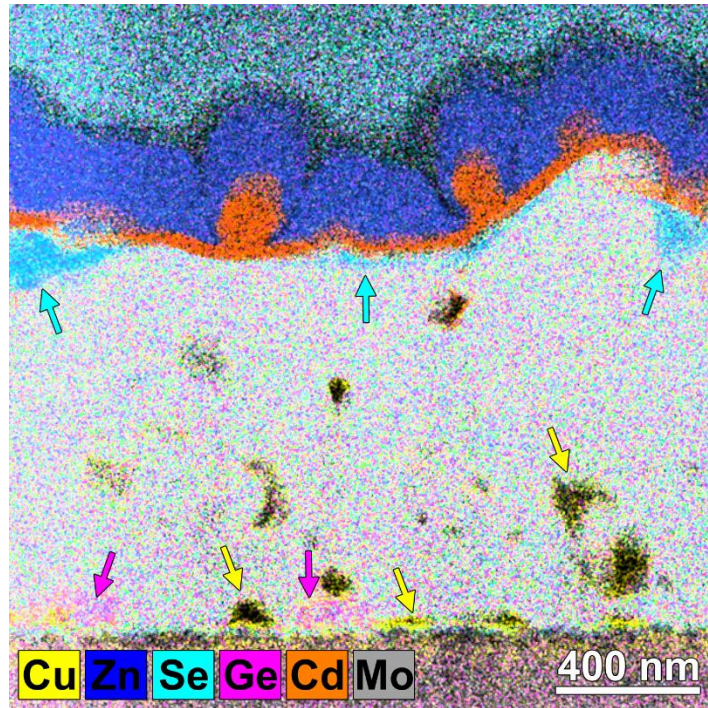


1
 2 Figure 1: Hard x-ray photoelectron survey spectra of an EVAP- Cu_8SiS_6 sample before (black)
 3 and after (red) sulfurization treatment (spectra are offset for clarity). Due to the
 4 sulfurization, the oxygen and sodium (most likely diffused from the soda-lime glass
 5 substrate) contents increase. The inset shows the region of the Si 2s and S 2p core level
 6 lines compared to reference positions [12] of silicon compounds (note that the order of
 7 appearance is different compared to the survey spectra for better visibility). The S 2p line
 8 can only be clearly observed on a magnified (x 25) scale.
 9



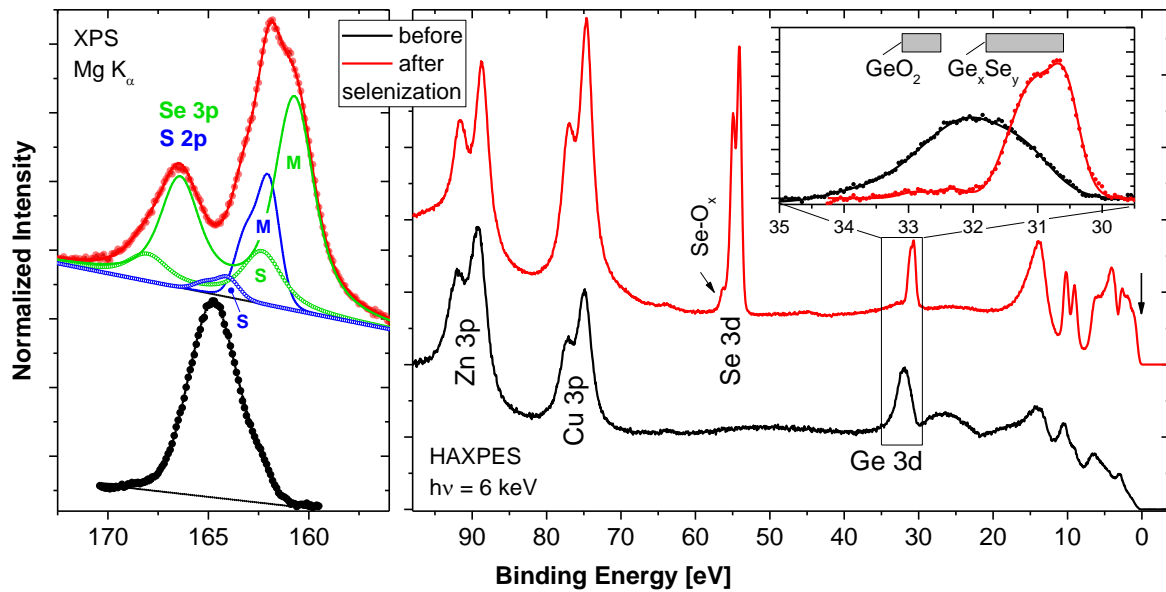
1
2
3
4
5

Figure 2: X-ray diffraction pattern of the EVAP-Cu₂ZnGeSe₄ absorber layer fabricated by selenizing the precursor stack for 15 min at 460°C on a Mo back contact together with reference positions for Cu₂ZnGeSe₄ and Mo (PDF card 00-052-0867).



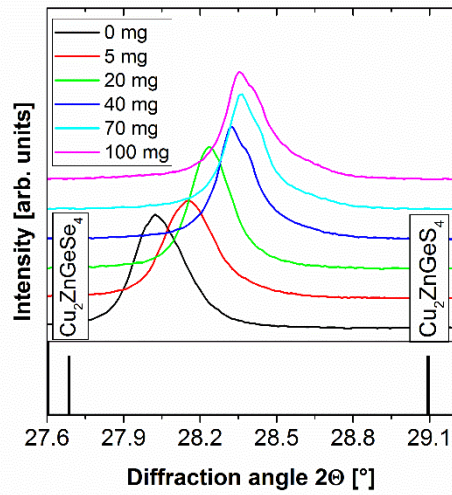
1
2
3
4
5
6
7

Figure 3: Cross-section STEM-EDX elemental map of a complete EVAP-Cu₂ZnGeSe₄ solar cell sample with CdS buffer layer and ZnO window, showing in some regions inhomogeneous elemental distributions, most likely caused by secondary phases. Regions attributed to ZnSe- (blue arrows), Cu₂GeSe₃- (pink arrows), and Cu_{2-x}Se-like (yellow arrows) phases are indicated. See also [13].



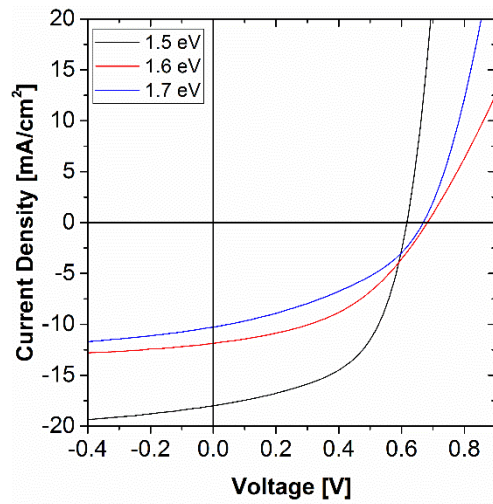
1
2
3
4
5
6
7
8
9

Figure 4: XPS (left panel) and HAXPES (right panel) S 2p/Se 3p and shallow core level spectra, respectively, of a SOL-Cu $_2$ ZnGe(S,Se) $_4$ absorber before (black) and after (red) Se-annealing induced absorber formation (spectra are offset for clarity). For the S 2p / Se 3p spectrum of the sample after selenization the respective fits of the S 2p (blue) and Se 3p (green) doublets are also shown. (M – main species, S – secondary species). The inset in the right panel shows the region of the Ge 3d shallow core level compared to reference positions for germanium compounds [12].



1
2
3
4

Figure 5: 112-reflection of XRD patterns from SOL-Cu₂ZnGe(S,Se)₄ absorbers processed in the presence of different amounts of GeS (0-100 mg).



1
2
3
4
5
6

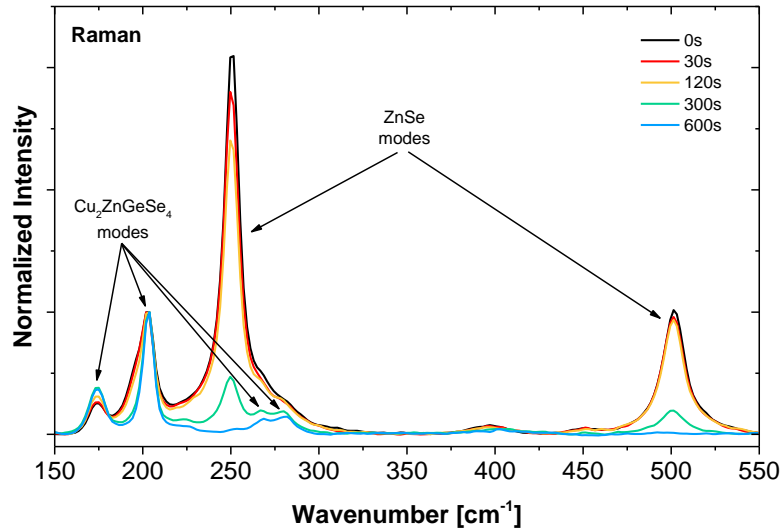
Figure 6: $J(V)$ -characteristics of the best solar cells that were prepared from SOL- $\text{Cu}_2\text{ZnGe}(\text{S},\text{Se})_4$ absorbers with band gaps of 1.5, 1.6, and 1.7 eV, respectively, as determined from EQE. The corresponding $[\text{S}]/([\text{S}]+[\text{Se}])$ -ratios are 0.27, 0.39, and 0.50.

E_G (eV)	1.5	1.6	1.7
Eff. (%)	6.0	3.6	2.7
V_{OC} (mV)	617	683	669
J_{SC} (mA/cm ²)	18.0	11.9	10.3
FF (%)	54.1	44.1	39.7

1

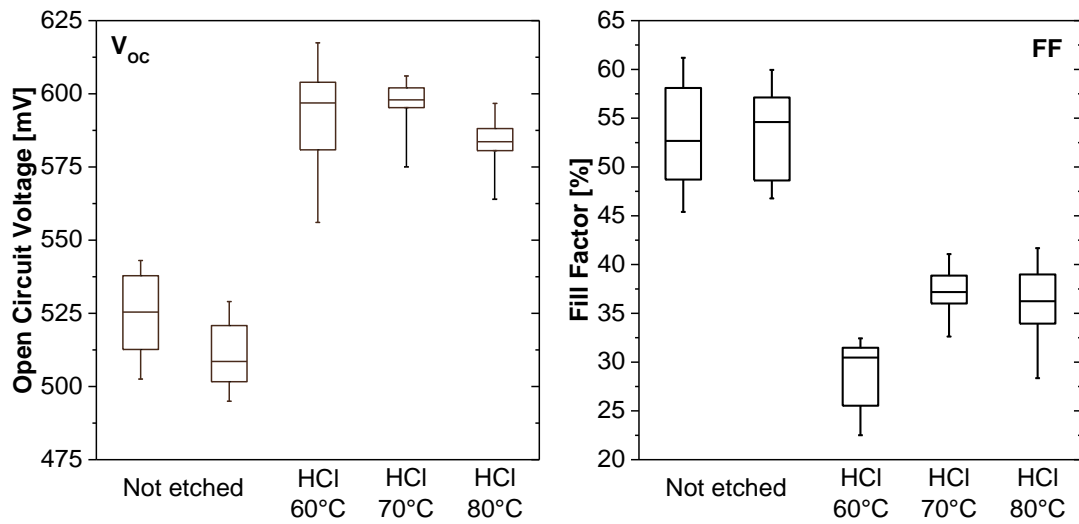
2 Table I: Solar cell parameters of solar cells with SOL-Cu₂ZnGe(S,Se)₄ absorbers with band
3 gaps of 1.5, 1.6, and 1.7 eV, respectively.

4



1
2
3
4
5
6

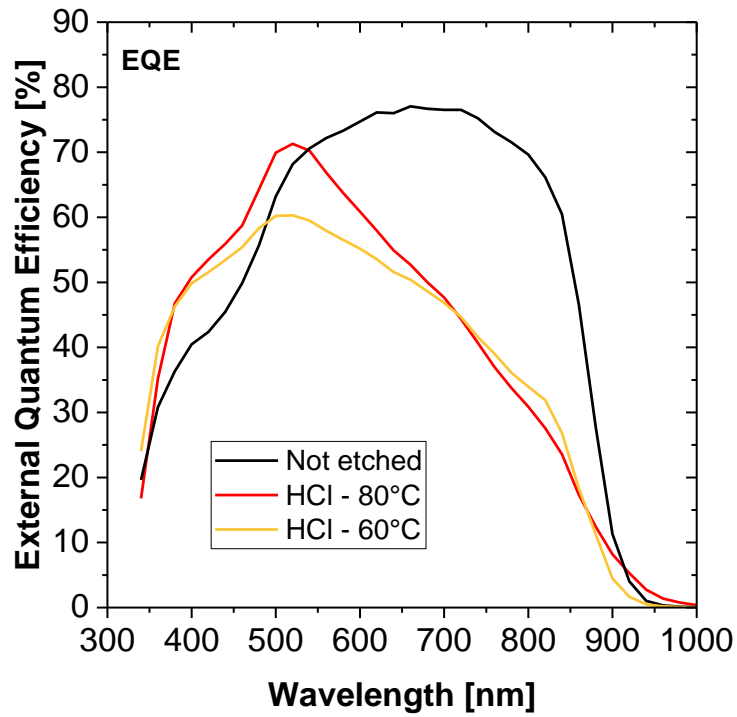
Figure 7: Raman spectra recorded with an excitation wavelength of 458 nm of EVAP-Cu₂ZnGeSe₄ samples that underwent HCl etching (T = 75°C, 12 wt% HCl) for different durations (from 0 to 600 s). Intensities are normalized to the most intense Cu₂ZnGeSe₄ peak ($\approx 204 \text{ cm}^{-1}$).



1

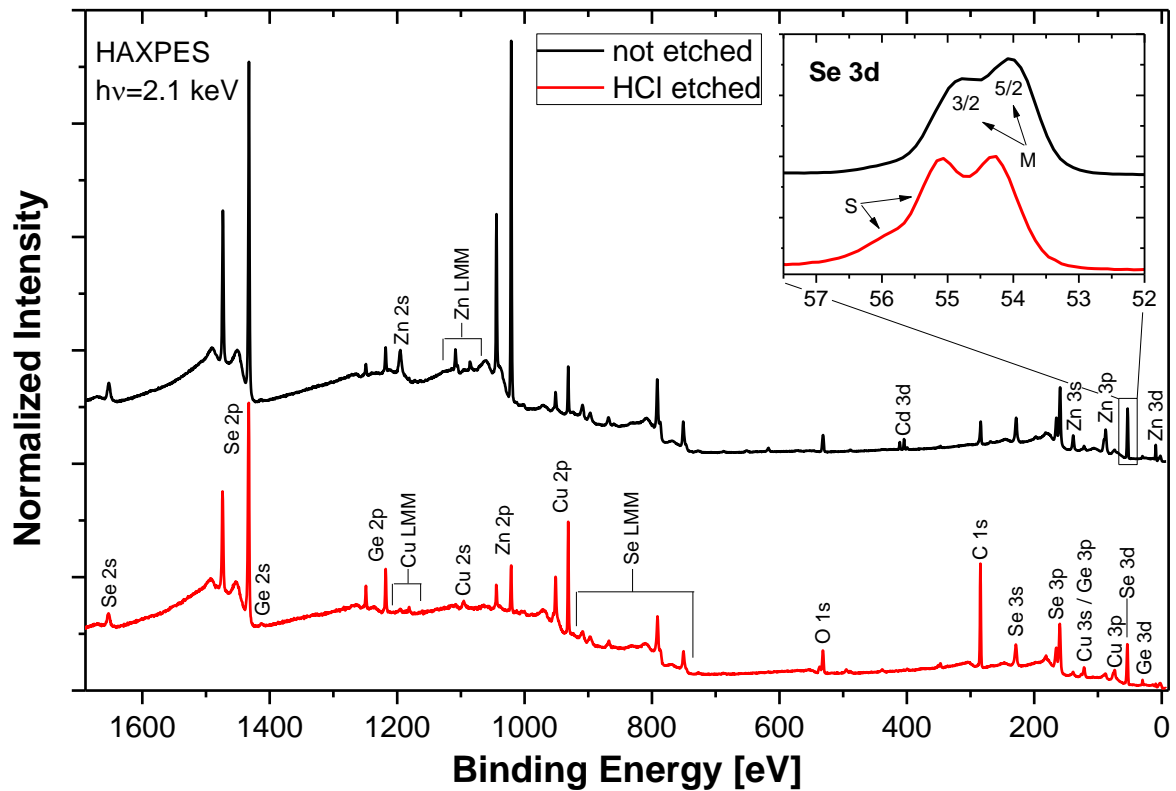
2 Figure 8: V_{oc} and FF mean values of EVAP- $Cu_2ZnGeSe_4$ based solar cells prepared using not-
 3 etched absorbers and absorbers HCl etched (using a 12 wt% HCl solution) at different
 4 temperatures (60 min at 60°C, 40 min at 70°C, 15 min at 80°C; 8-12 cells per sample, solar
 5 cell area $\approx 0.5 \text{ cm}^2$).

6

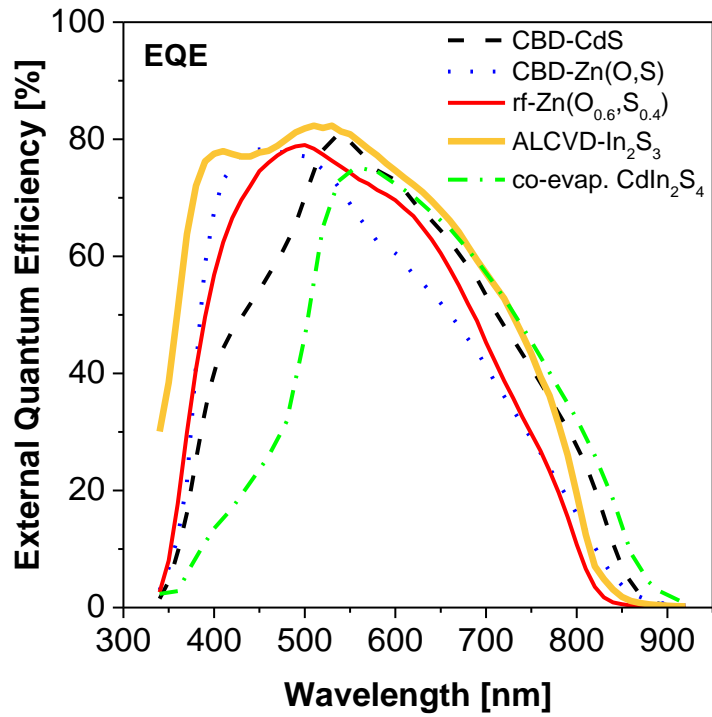


1
2
3
4
5
6

Figure 9: Representative EQE spectra of EVAP-Cu₂ZnGeSe₄ solar cells based on not-etched absorbers and absorbers HCl etched (using a 12 wt% HCl solution) at different temperatures (60 min at 60°C, 15 min at 80°C).



1
 2 Figure 10: HAXPES survey spectra of an as-deposited / not etched (black spectrum) and
 3 HCl etched (red spectrum) EVAP-Cu₂ZnGeSe₄ absorber. Spectra are offset for clarity and
 4 all prominent lines are labelled. Inset: Detail spectra of the related Se 3d energy region, with
 5 the 3/2 and 5/2 spin-orbit split doublet indicated. Further, the approximate positions of the
 6 Se 3d_{3/2} and 3d_{5/2} lines of the main (“M”) and secondary (“S”) selenium species are depicted.
 7



1
2
3
4
5

Figure 11: Representative EQE spectra of solar cells with SOL-Cu₂ZnGe(S,Se)₄ absorber and different buffer layers: sputtered (rf) Zn(O_{0.6}S_{0.4}), CBD-Zn(O,S), CBD-CdS, atomic layer chemical vapor deposited (ALCVD) In₂S₃, and co-evaporated (“co-evap.”) CdIn₂S₄.

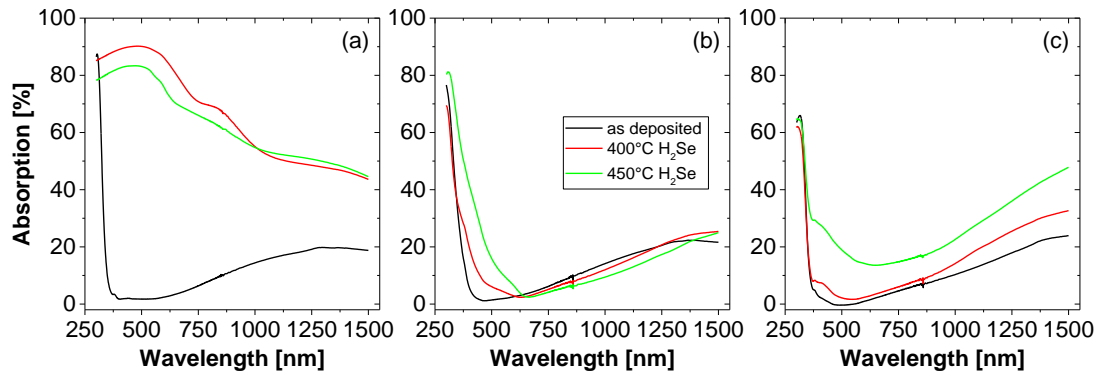
Solar cell parameters	Cell configurations			
	(a)	(b)	(c)	(d)
Back contact	MoSe ₂ /Mo	MoSe ₂ /Mo ^(○)	TCO ^(○)	MoO ₃ /TCO ^(○)
V _{OC} (mV)	553	572	287	1000
J _{SC} (mA/cm ²)	19.70	20.00	17.60	22.00
FF (%)	56.30	71.00	65.54	67.90
Eff. (%)	6.22	8.14	3.31	15.00

1

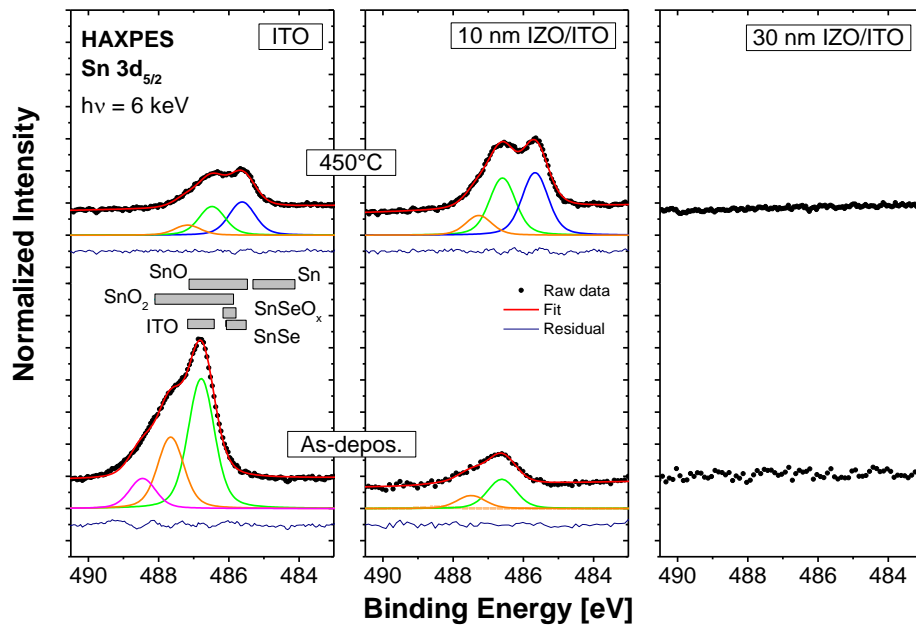
2 Table 2: Solar cell parameters calculated for the different configurations as derived from the
3 J(V) data shown in Figure S6. ^(○) Results from device simulation employing optimized
4 parameters (see Table S2).

5

6



1
 2 Figure 12: Absorption of ITO without (a) and with a 30 nm IZO (b), and with a 60 nm TiO₂
 3 (c) protective top layer before (i.e., as-deposited) and after H₂Se exposure at 400 and
 4 450°C.



1
2
3
4
5
6

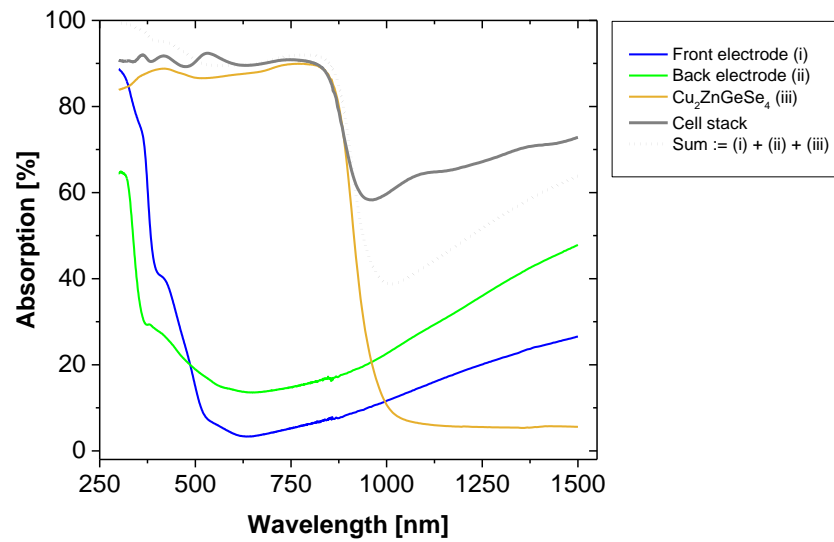
Figure 13: Sn $3d_{5/2}$ HAXPES spectra of the ITO, 10 nm, and 30 nm IZO/ITO samples before (“As-depos.”) and after H_2Se treatment at 450 °C. The curve fit was done by using one linear background and three Voigt profiles. The grey boxes indicate the Sn $3d_{5/2}$ energetic position for reference compounds [12].

Back contact	Protective top layer	Eff. _{max} (%)	J _{sc} (mA/cm ²)	V _{oc} (mV)	FF (%)
ITO	None	3.6	19.9	487	37.6
ITO	IZO (30 nm)	4.0	27.1	471	31.2
ITO	Al ₂ O ₃ (3.5 nm)	0.8	9.3	364	23.9
ITO	TiO ₂ (30 nm)	4.3	17.3	600	41.3
SiON/Mo	None	4.7	18.6	600	42.3

1

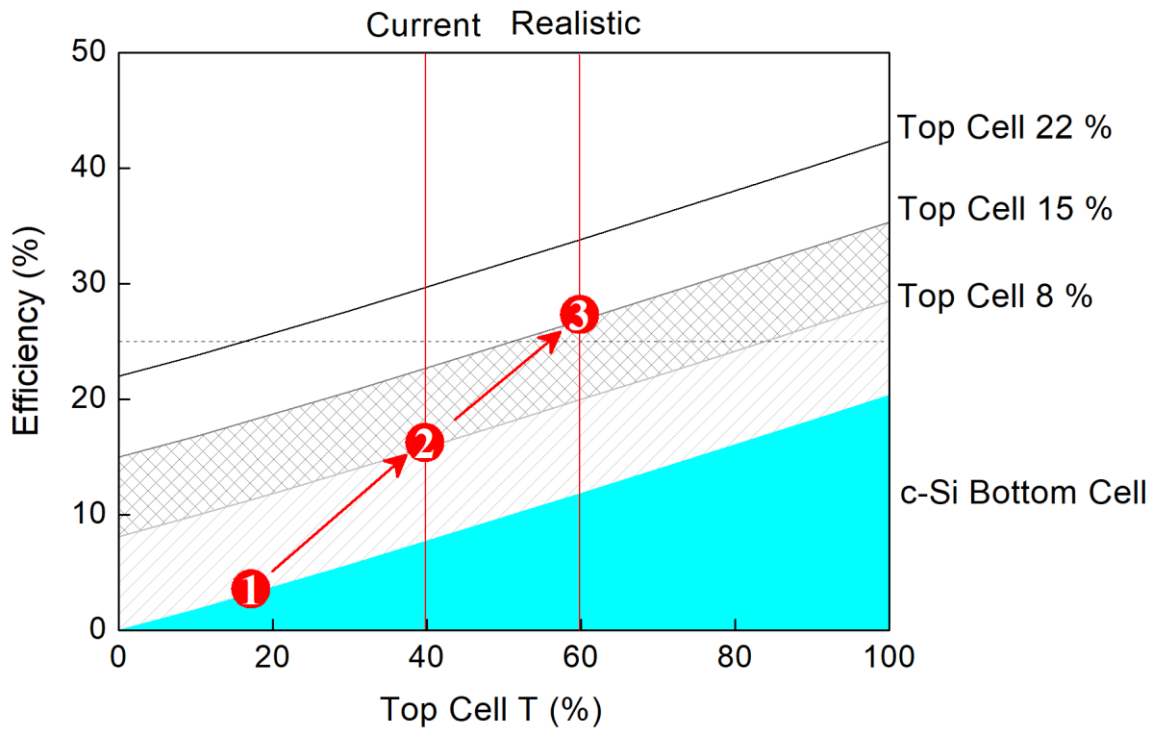
2 Table 3: Overview of the J(V) parameters of the manufactured EVAP-Cu₂ZnGeSe₄ devices
3 (best cells).

4



1
2
3
4
5
6
7

Figure 14: Absorption spectra of the (complete) front electrode/EVAP-Cu₂ZnGeSe₄/60 nm TiO₂/ITO cell stack and of the individual stack components: (i) ZnO:Al front electrode, (ii) 60 nm TiO₂/ITO back electrode after H₂Se exposure at 450°C, (iii) EVAP-Cu₂ZnGeSe₄ absorber (as-deposited on quartz glass substrate) compared to their spectral sum := (i) + (ii) + (iii).



1
 2 Figure 15: The efficiency of a four-terminal mechanically stacked geometry c-Si bottom+top
 3 cell as function of the light transmitted through the top cell (T for $\lambda \geq hc/E_{g_{top}}$). As top cell,
 4 8 and 15 % CZGSe and 22 % CIGS cells are used. The horizontal dashed line indicates the
 5 efficiency of the c-Si bottom cell alone and serves as a performance reference. ❶ and ❷
 6 indicate the performance situation in 2015 ($\eta \approx 3\%$ and $T \approx 17\%$, calculated for measured
 7 transparency of CZGSe on TBC (ITO/TiO₂)) and 2018 (as reported in this publication: $\eta \approx$
 8 8% and $T \approx 40\%$). ❸ indicates a realistic performance scenario for which η and T have to
 9 be increased to 15% and 60% , respectively.

10

1 **SUPPLEMENTARY MATERIAL FOR**

2
3 **WIDE BAND GAP KESTERITE ABSORBERS FOR THIN FILM SOLAR CELLS:**
4 **POTENTIAL AND CHALLENGES FOR THEIR DEPLOYMENT IN TANDEM DEVICES**

5
6 Bart Vermang^{1,2,3}, Guy Brammertz^{1,2,3}, Marc Meuris^{1,2,3}, Thomas Schnabel⁴, Erik Ahlswede⁴,
7 Leo Choubrac⁵, Sylvie Harel⁵, Christophe Cardinaud⁵, Ludovic Arzel⁵, Nicolas Barreau⁵,
8 Joop van Deelen⁶, Pieter-Jan Bolt⁶, Patrice Bras⁷, Yi Ren⁷, Eric Jaremalm⁷, Samira Khelifi^{8,9},
9 Sheng Yang⁸, Johan Lauwaert⁸, Maria Batuk¹⁰, Joke Hadermann¹⁰, Xeniya Kozina¹¹,
10 Evelyn Handick¹¹, Claudia Hartmann¹¹, Dominic Gerlach¹², Asahiko Matsuda¹³,
11 Shigenori Ueda^{14,15}, Toyohiro Chikyow^{12,13}, Roberto Félix¹¹, Yufeng Zhang^{11,16},
12 Regan G. Wilks^{11,17}, and Marcus Bär^{11,17,18,19}

13
14 ¹imec division IMOMEc – partner in Solliance, Wetenschapspark 1, 3590 Diepenbeek,
15 Belgium

16 ²Hasselt University – partner in Solliance, Martelarenlaan 42, 3500 Hasselt, Belgium

17 ³EnergyVille, Thorpark 8320, 3600 Genk, Belgium

18 ⁴ZSW, Meitnerstrasse 1, 70563 Stuttgart, Germany

19 ⁵Institut des Matériaux Jean Rouxel (IMN), Université de Nantes, CNRS, 2 rue de la
20 Houssinière, 44322 Nantes, France

21 ⁶TNO – partner in Solliance, High Tech Campus 21, 5656 AE Eindhoven, The Netherlands

22 ⁷Midsummer AB, Elektronikhöjden 6, 175 43 Järfälla, Sweden

23 ⁸Department of Electronics and Information Systems (ELIS), Ghent University,
24 Technologiepark Zwijnaarde 15, 9052 Gent, Belgium

25 ⁹Department of Solid State Sciences, Ghent University, Krijgslaan 281-S1, 9000 Gent,
26 Belgium

27 ¹⁰Electron Microscopy for Materials Science (EMAT), University of Antwerp,
28 Groenenborgerlaan 171, 2020 Antwerp, Belgium

29 ¹¹Department Interface Design, Helmholtz-Zentrum Berlin für Materialien und Energie
30 GmbH (HZB), Hahn-Meitner-Platz 1, 14109 Berlin, Germany

1 ¹²International Center for Materials Nanoarchitectonics (MANA), National Institute for
2 Materials Science (NIMS), 1-1 Namiki, Tsukuba, Ibaraki 305-0044, Japan

3 ¹³Research and Services Division of Materials Data and Integrated System (MaDIS), National
4 Institute for Materials Science (NIMS), 1-1 Namiki, Tsukuba, Ibaraki 305-0044, Japan

5 ¹⁴Synchrotron X-ray Station at SPring-8, National Institute for Materials Science (NIMS), 1-1-
6 I Kouto, Sayo-cho, Hyogo 679-5148, Japan

7 ¹⁵Research Center for Advanced Measurement and Characterization, National Institute for
8 Materials Science (NIMS), 1-2-1, Sengen, Tsukuba, Ibaraki 305-0047, Japan

9 ¹⁶College of Physical Science and Technology, Xiamen University (XMU), 361005, Xiamen,
10 China

11 ¹⁷Energy Materials In-Situ Laboratory Berlin (EMIL), Helmholtz-Zentrum Berlin für
12 Materialien und Energie GmbH (HZB), Albert-Einstein-Str. 15, 12489, Berlin, Germany

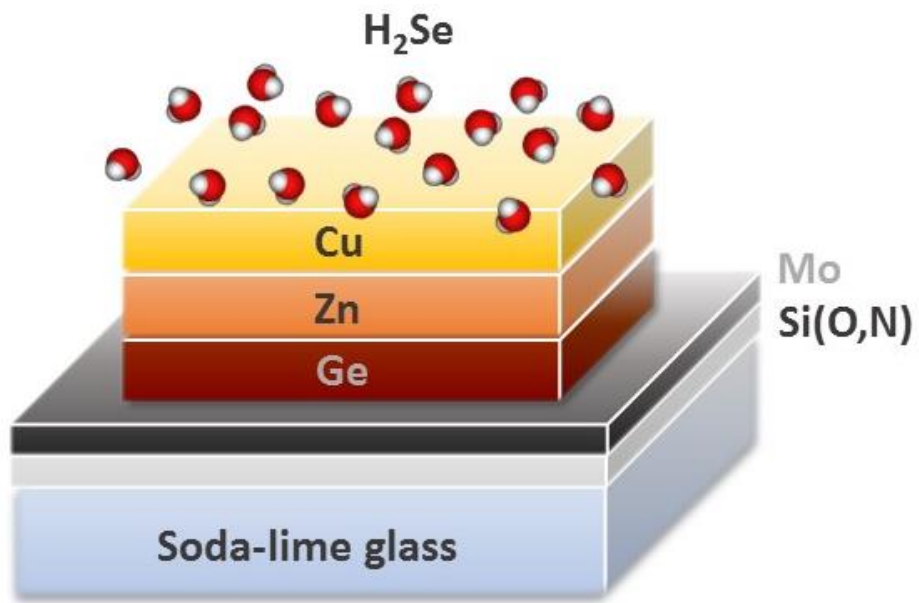
13 ¹⁸Department of Chemistry and Pharmacy, Friedrich-Alexander-Universität Erlangen-
14 Nürnberg, 91058 Erlangen, Germany

15 ¹⁹Helmholtz-Institute Erlangen-Nürnberg for Renewable Energy (HI ERN),
16 Forschungszentrum Jülich, 91058 Erlangen, Germany

17

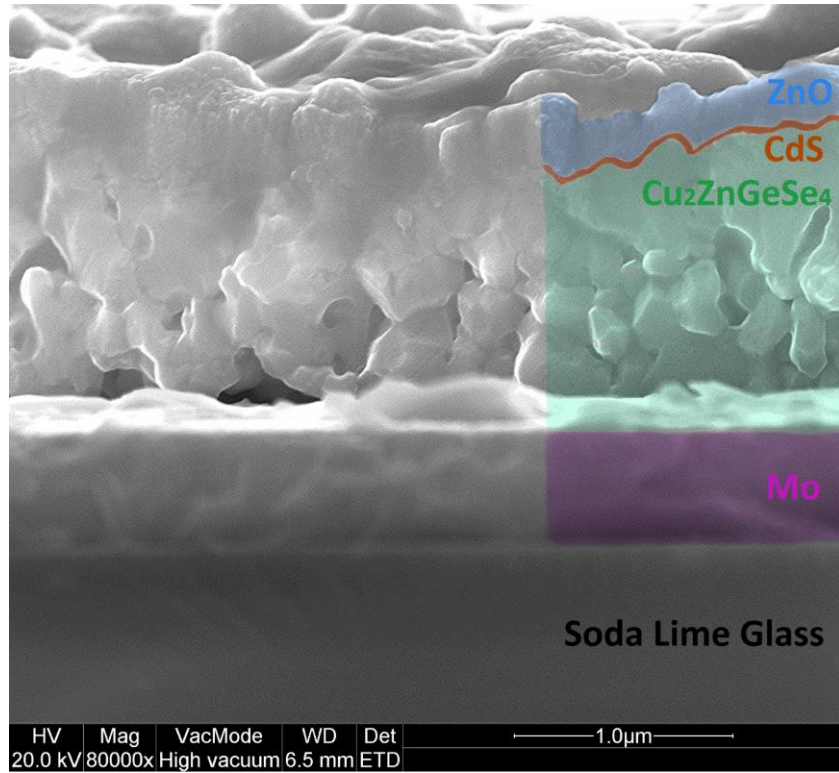
18 CORRESPONDING AUTHOR – Bart Vermang, Martelarenlaan 42, 3500 Hasselt, Belgium

19

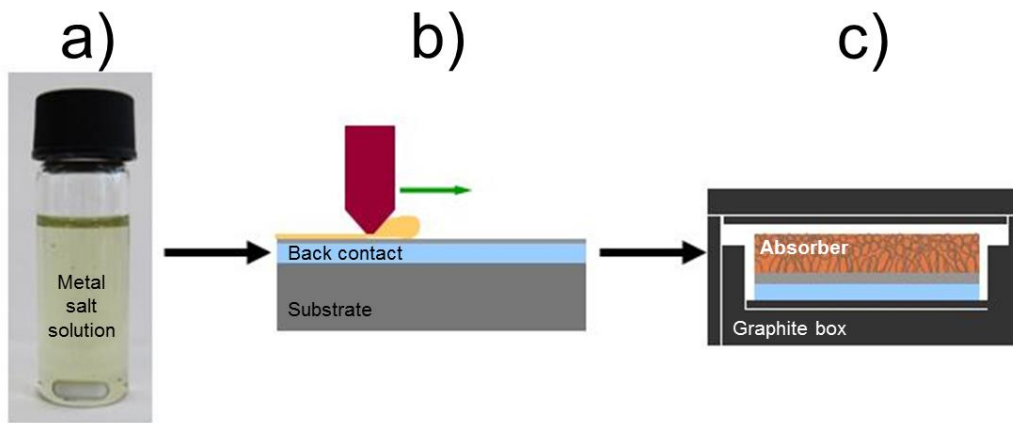


1
2
3
4

Figure S1: Schematic representation of the two-step selenization process used for EVAP-Cu₂ZnGeSe₄ absorber fabrication.



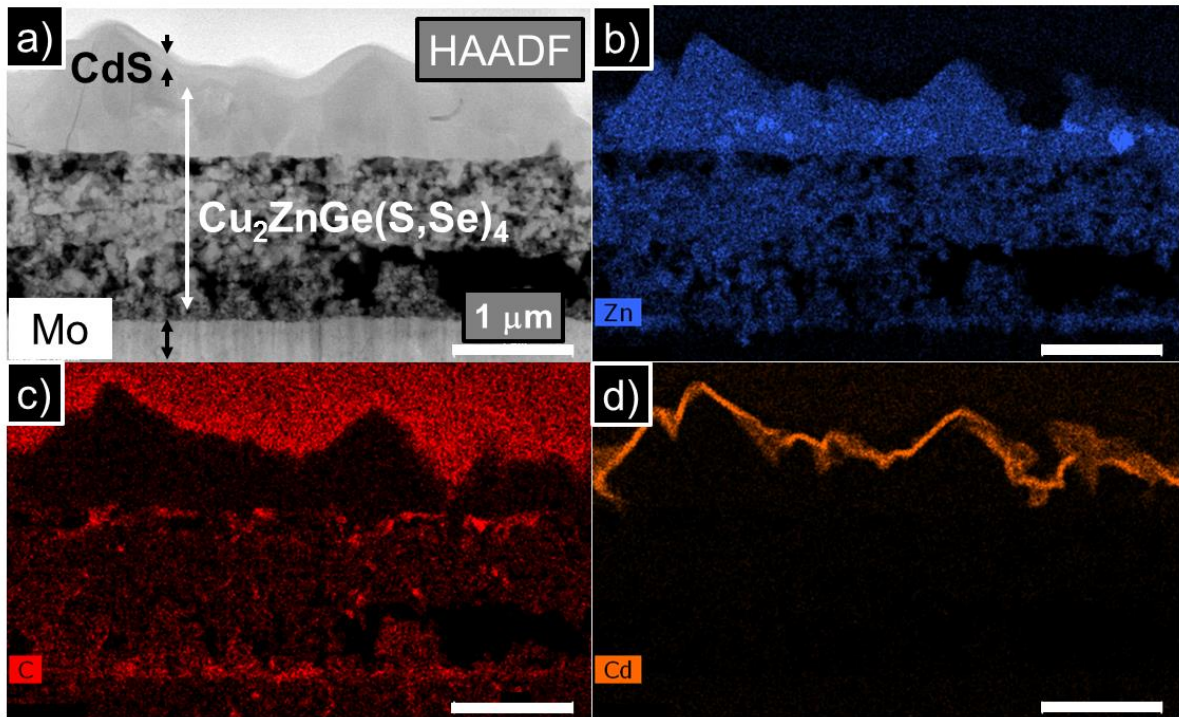
1
2 Figure S2: Cross-section scanning electron microscopy image of a finished EVAP-
3 $\text{Cu}_2\text{ZnGeSe}_4$ solar cell sample, showing the grain morphology of the absorber and contact
4 layer.
5



1

2 Figure S3: Schematic illustration of the solution process of preparing a SOL-Cu₂ZnGe(S,Se)₄
 3 absorber: a) metal salt solution, b) doctor blade coating, c) annealing in Se atmosphere.

4



1
2
3
4
5

Figure S4: Cross-section high angle annular dark field (HAADF) STEM image of a SOL- $\text{Cu}_2\text{ZnGe}(\text{S},\text{Se})_4$ -based solar cell with CdS buffer and ZnO window (a), and the elemental maps of Zn (b), C (c) and Cd (d).

Buffer layer	V_{OC} (mV)	FF (%)	J_{sc} (mA/cm ²)	E_G (eV)	Eff. (%)
CBD CdS ^[17]	617	54.1	18.0	1.47	6.0
CBD Zn(O,S)	512	51.2	17.7	1.51	4.6
rf-Zn(O _{0.6} S _{0.4}) ^[17]	730	48.3	13.0	1.54	4.6
ALCVD In ₂ S ₃ ^[17]	469	48.2	14.9	1.49-1.54	3.4
Co-evap. CdIn ₂ S ₄ ^[17]	354	49.6	14.7	1.44	2.6

1

2 Table S1: Electrical parameters for the most efficient buffer/SOL-Cu₂ZnGe(S,Se)₄ solar cells.

3

Parameter	ZnO:Al	CdS	Cu ₂ ZnGe(S,Se) ₄	MoSe ₂ ^[31]	MoO ₃ ^[32]
d (μm)	0.120	0.050	1-2	0.04-0.10	0.04
E _G (eV)	3.3	2.4	1.47-1.5	1.1	2.85
χ (eV)	4.4	4.2	4.54	4.14	2.6
μ _n (cm ² /V.s)	100	100	10	100	100
μ _p (cm ² /V.s)	25	25	2	25	20
N _d (cm ⁻³)	10 ¹⁸	3×10 ¹⁷	-	-	-
N _A (cm ⁻³)	-	-	2×10 ¹⁵ / 10 ¹⁶ ^(○)	10 ¹⁶	10 ¹⁸
R _s (Ω.cm ⁻¹)	4.7 / 0.5 ^(○)				
R _{sh} (Ω.cm ⁻¹)	365 / 800 ^(○)				

1

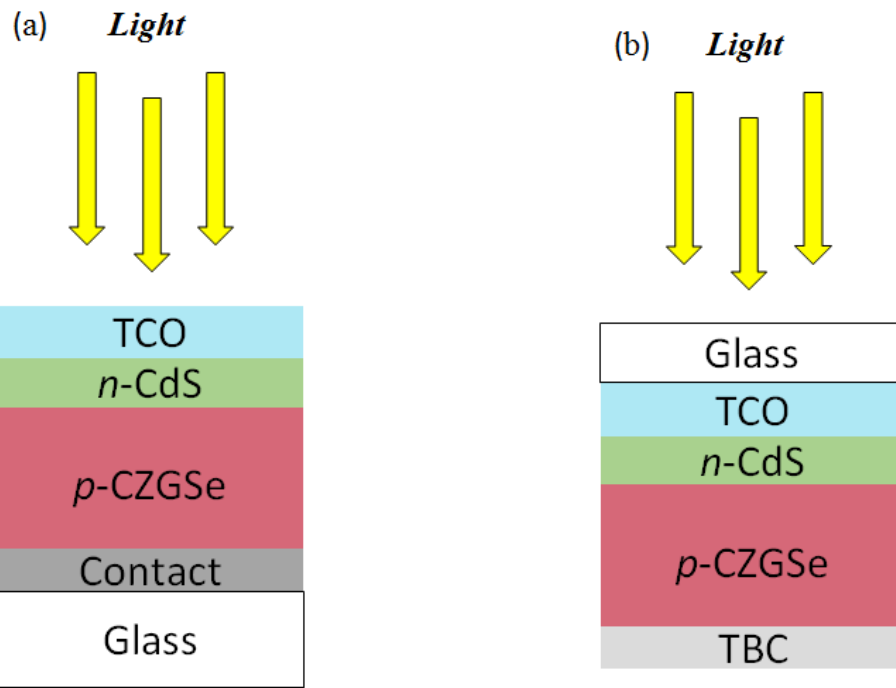
2

Table S2: Parameters used in the simulations at standard solar cell test conditions.

3

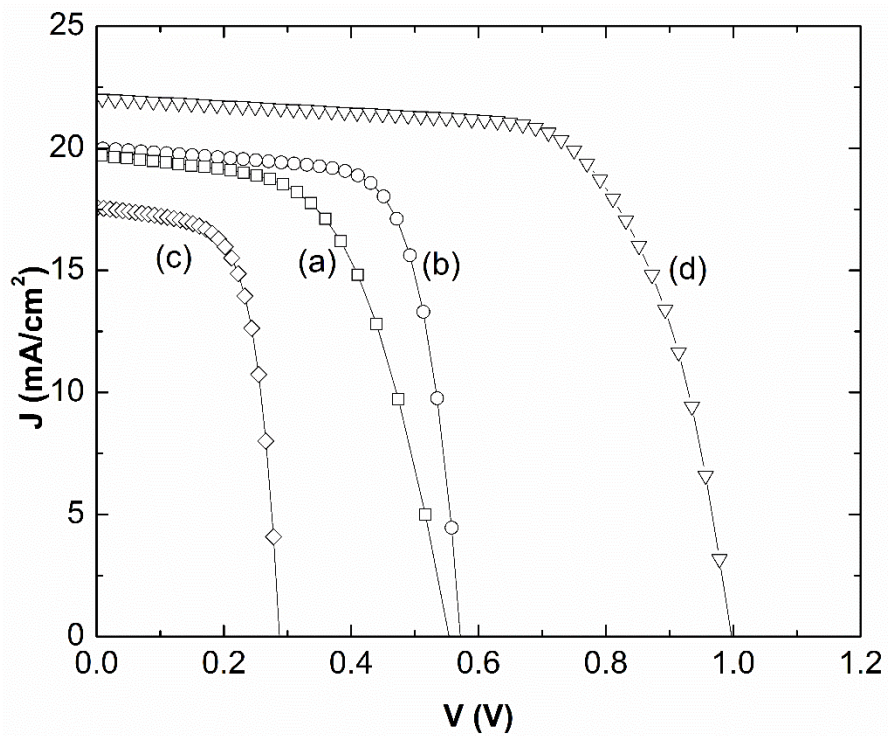
^(○) Optimized parameters.

4



1
2
3
4

Figure S5: Schematic of the two different configurations considered in the device simulations: (a) substrate and (b) superstrate.



1

2 Figure S6: Calculated $J(V)$ curves for different substrate/superstrate configurations: (a)

3 substrate = $\text{Cu}_2\text{ZnGe}(\text{S},\text{Se})_4/\text{MoSe}_2/\text{Mo}/\text{glass}$, (b) same configuration as (a) but using

4 optimized device simulation parameters (see Table S2), (c) superstrate =

5 $\text{Cu}_2\text{ZnGe}(\text{S},\text{Se})_4/\text{TCO}$, and (d) superstrate = $\text{Cu}_2\text{ZnGe}(\text{S},\text{Se})_4/\text{MoO}_3/\text{TCO}$. For

6 configurations (c) and (d) also optimized parameters were used in the device simulation.

7